Monthly Notices
of the
ROYAL ASTRONOMICAL SOCIETY

MNRAS **481,** 1726–1743 (2018)
Advance Access publication 2018 September 4

doi:10.1093/mnras/sty2403

Aurigaia: mock *Gaia* DR2 stellar catalogues from the AURIGA cosmological simulations

Robert J. J. Grand,[1,2]★ John Helly,[3] Azadeh Fattahi,[3] Marius Cautun,[3] Shaun Cole,[3] Andrew P. Cooper,[3] Alis J. Deason,[3] Carlos Frenk,[3] Facundo A. Gómez,[4,5,6] Jason A. S. Hunt,[7] Federico Marinacci,[8,9] Rüdiger Pakmor,[1] Christine M. Simpson,[1] Volker Springel[1,2,6] and Dandan Xu[1]

[1]*Heidelberger Institut für Theoretische Studien, Schloss-Wolfsbrunnenweg 35, D-69118 Heidelberg, Germany*
[2]*Zentrum für Astronomie der Universität Heidelberg, Astronomisches Recheninstitut, Mönchhofstr. 12-14, D-69120 Heidelberg, Germany*
[3]*Department of Physics, Institute for Computational Cosmology, Durham University, South Road, Durham DH1 3LE, UK*
[4]*Instituto de Investigación Multidisciplinar en Ciencia yTecnología, Universidad de La Serena, Raúl Bitrán 1305, La Serena, Chile*
[5]*Departamento de Física y Astronomía, Universidad de LaSerena, Av. Juan Cisternas 1200 N, La Serena, Chile*
[6]*Max-Planck-Institut für Astrophysik, Karl-Schwarzschild-Str. 1, D-85748 Garching, Germany*
[7]*Dunlap Institute for Astronomy and Astrophysics, University of Toronto, 50 St. George Street, Toronto, Ontario M5S 3H4, Canada*
[8]*Department of Physics, Kavli Institute for Astrophysics and Space Research, MIT, Cambridge, MA 02139, USA*
[9]*Harvard-Smithsonian Center for Astrophysics, 60 Garden Street, Cambridge, MA 02138, USA*

Accepted 2018 August 31. Received 2018 July 31; in original form 2018 April 23

ABSTRACT

We present and analyse mock stellar catalogues that match the selection criteria and observables (including uncertainties) of the *Gaia* satellite data release 2 (DR2). The source are six cosmological high-resolution magneto-hydrodynamic ΛCDM zoom simulations of the formation of Milky Way analogues from the AURIGA project. Mock data are provided for stars with $V < 16$ mag and $V < 20$ mag at $|b| > 20$ deg. The mock catalogues are made using two different methods: the public SNAPDRAGONS code, and a method based on that of Lowing et al. (2015) that preserves the phase-space distribution of the model stars. These publicly available catalogues contain five-parameter astrometry, radial velocities, multiband photometry, stellar parameters, dust extinction values, and uncertainties in all these quantities. In addition, we provide the gravitational potential and information on the origin of each star. By way of demonstration, we apply the mock catalogues to analyses of the young stellar disc and the stellar halo. We show that (i) the young outer stellar disc exhibits a flared distribution that is detectable in the height and vertical velocity distribution of A- and B-dwarf stars up to radii of ∼15 kpc, and (ii) the spin of the stellar halo out to 100 kpc can be accurately measured with *Gaia* DR2 RR Lyrae stars. These catalogues are well suited for comparisons with observations and should help to (i) develop and test analysis methods for the *Gaia* DR2 data, (ii) gauge the limitations and biases of the data, and (iii) interpret the data in the light of theoretical predictions from realistic *ab initio* simulations of galaxy formation in the ΛCDM cosmological model.

Key words: galaxies: evolution – galaxies: kinematics and dynamics – galaxies: spiral – galaxies: structure.

1 INTRODUCTION

Over the next five years, our view of the Milky Way galaxy will be revolutionized by the European Space Agency's cornerstone *Gaia* mission (Gaia Collaboration 2016), which aims to provide positions and velocities for billions of stars in the Galaxy – a 10 000-fold increase in sample size and 100-fold increase in precision over its predecessor, *Hipparcos* (van Leeuwen et al. 2007). The second *Gaia* date release (DR2, Gaia Collaboration 2018a,b,c) will already provide astrometric and photometric data in three bands for ∼1.4 billion sources over the entire sky. A fraction of this data set will contain

★ E-mail: Robert.Grand@h-its.org

also measurements for radial velocities, extinction, and effective temperatures. With subsequent *Gaia* data releases, in combination with several major current and future spectroscopic surveys, such as SDSS/APOGEE (Majewski et al. 2017), DESI (DESI Collaboration 2016), Gaia-ESO (Gilmore et al. 2012), LAMOST (Chen et al. 2012), GALAH (Martell et al. 2017) and 4MOST (de Jong et al. 2014), and asteroseismic surveys, such as K2 (Stello et al. 2017), TESS (Campante et al. 2016), and PLATO (Rauer et al. 2014), additional data for tens of millions of stars will become available that include chemical abundances, radial velocities, and stellar ages.

In principle, this huge amount of high-dimensional empirical information about the stellar component of our Galaxy holds the key to unveiling its current state through precise identification of disc, bulge, and halo substructure, and its formation history (see Rix & Bovy 2013, for a recent overview). Given that the Milky Way is thought to be fairly typical for its mass (although see Bell et al. 2017; Cautun et al., in preparation) within the standard model of cosmology – the Lambda Cold Dark Matter (ΛCDM) paradigm – this multidimensional star-by-star information provides a unique window into the formation of L_* galaxies in general as well as a test of the predictions of ΛCDM.

This new wealth of observational data is only a partial snapshot of the current distribution of stars in our quadrant of the Milky Way, however, and its interpretation requires some form of modelling. Widely employed modelling techniques include dynamical models such as (quasi-) distribution functions (Binney 2010; Bovy & Rix 2013; Trick, Bovy & Rix 2016), Torus mapping (Binney & McMillan 2016), Made-to-Measure (M2M) models (Syer & Tremaine 1996; Hunt & Kawata 2013) that aim to characterize the current structure of the major Galactic components, and self-consistent *N*-body models that provide testable predictions for the effects of various evolutionary processes (e.g. Grand, Kawata & Cropper 2012; Fragkoudi et al. 2017; Kawata et al. 2017). A crucial aspect in the quest to draw reliable conclusions from any of these techniques is to understand the limitations, biases, and quality of the observational data. Specifically, the effects of survey selection functions, sample size, survey volume, accuracy of phase-space and spectroscopic measurements, dust obscuration, and image crowding influence inferences as to the true phase-space distribution of stars.

A pragmatic solution to these problems is to generate and analyse synthetic Milky Way catalogues cast in the observational frame of the survey (Bahcall & Soneira 1980; Robin & Creze 1986; Bienayme, Robin & Creze 1987). 'Mock catalogues' of this general type were first used in cosmology in the 2000s (e.g. Cole et al. 2005) and have now become an essential tool for the design and analysis of large galaxy and quasar surveys. Realistic mock catalogues provide assessments of an instrument's capabilities and biases, tests of statistical modelling techniques applied to realistic representations of observational data, and detailed comparisons between theoretical predictions and observations. Perhaps one of the best known recent attempts is the Besançon model (Robin et al. 2003), which provides a disc (or set of discs) with a set of coeval and isothermal (single velocity dispersion) stellar populations assumed to be in equilibrium, with analytically specified distributions of density, metallicity, and age. This has been the basis of the *Gaia Universe Model* (GUMS; Robin et al. 2012). However, these models are not dynamically consistent and oversimplify the structure of the Galaxy, particularly the stellar halo that is modelled as a smooth component. An important advance was made by Sharma et al. (2011), who developed the GALAXIA code for creating mock stellar catalogues either analytically or from phase-space sampling of hybrid semi-analytic-*N*-body simulations to represent stellar haloes in a cosmological context (Bullock & Johnston 2005; Cooper et al. 2010). Rybizki et al. (2018) have developed a mock catalogue designed specifically for *Gaia* DR2 based on GALAXIA. Building on the method of Sharma et al. (2011), Lowing et al. (2015) developed a technique to distribute synthetic stars sampled from a cosmological *N*-body simulation in such a way as to preserve the phase-space properties of their parent stellar populations. In a separate method, Hunt et al. (2015) introduced the SNAPDRAGONS code that generates a mock catalogue taking into account *Gaia* errors and extinction and demonstrated the resulting observable kinematics of stars around a spiral arm in an idealized smoothed particle hydrodynamic simulation set-up in isolation.

One of the goals of modern Galactic astronomy is to compare predictions of *ab initio* cosmological formation models with the high-dimensional observational data provided by Galactic surveys in order to elucidate the evolutionary history of the Galaxy. Mock stellar catalogues based on full hydrodynamical cosmological simulations are an appealing prospect to fulfil this aim. This would provide us with a window into how different types of stars that originate from cosmological initial conditions are distributed in phase space. Given that the details of these distributions will depend on the formation history of the Milky Way, multiple mock catalogues derived from simulations that span a range of formation histories will be desirable for many aspects of disc and halo formation.

Until recently, the availability of realistic cosmological simulations of Milky Way analogues has been limited due to a combination of numerical hindrances and insufficiently realistic astrophysical modelling of important physical effects, such as feedback processes (Katz & Gunn 1991; Navarro & Steinmetz 2000; Guo et al. 2010; Scannapieco et al. 2011). This situation has improved and cosmological zoom simulations have now become sophisticated enough to produce sets of high-resolution Milky Way analogues in statistically meaningful numbers (e.g. Marinacci, Pakmor & Springel 2014; Wang et al. 2015; Fattahi et al. 2016; Garrison-Kimmel et al. 2017). In particular, the AURIGA simulation suite (Grand et al. 2017) consists of 40 Milky Way mass haloes simulated at resolutions comparable to the most modern idealized simulations (6×10^3–5×10^4 $M_\odot$ per baryonic element) with a comprehensive galaxy formation model, including physical processes such as magnetic fields (Pakmor, Marinacci & Springel 2014) and feedback from active galactic nuclei (Springel, Di Matteo & Hernquist 2005) and stars (Vogelsberger et al. 2013). These simulations have been shown to produce disc-dominated, star-forming late-type spiral galaxies that are broadly consistent with a plethora of observational data such as star formation histories, abundance-matching predictions, gas fractions, sizes, and rotation curves of L_* galaxies (Grand et al. 2017). Furthermore, they are sufficiently detailed to address questions related to chemodynamic properties of the Milky Way, such as the origin of the chemical thin-thick disc dichotomy (Grand et al. 2018), the formation of bars, spiral arms and warps (Gómez et al. 2017), and the properties of the stellar halo (Monachesi et al. 2016, 2018) and satellite galaxies (Simpson et al. 2018). The confluence of these advanced simulation techniques with the new *Gaia* and ground-based data will transform, at a fundamental level, the understanding of our Galaxy in its cosmological context.

The aim of this paper is to present two sets of mock *Gaia* DR2 stellar catalogues generated from the AURIGA cosmological simulations: one set generated with a parallel version of SNAPDRAGONS (Hunt et al. 2015) denoted HITS-MOCKS, and another with the code presented in Lowing et al. (2015) denoted ICC-MOCKS. These catalogues contain the true and observed phase-space coordinates of stars, their *Gaia* DR2 errors, magnitudes in several passbands,

metallicities, ages, masses, and stellar parameters. We show that a powerful use of the mock catalogues is to compare them with the intrinsic simulation data from which they were generated in order to acquire predictions of how accurately physical properties are reproduced, and to determine which kind of data should be studied from the *Gaia* survey to target specific questions. We focus on two practical applications: the structure of the young stellar disc and kinematics of the stellar halo. In particular, we show that, in contrast to typical disc set-ups in many idealized *N*-body simulations, the AURIGA simulations predict that young stars (∼few hundred Myr old) make up flared distributions (increasing scale height with increasing radius), which are well traced by B- and A-dwarf stars. We also show that the systemic rotation of the stellar halo can be accurately inferred from *Gaia* data. Finally, we discuss the limitations of our methods and provide information on how the community can access the mock data.

2 MAGNETO-HYDRODYNAMICAL SIMULATIONS

The AURIGA simulations (Grand et al. 2017) are a suite of cosmological zoom simulations of haloes in the virial mass[1] range 10^{12}–2×10^{12} $M_\odot$. The haloes were identified as isolated haloes[2] from the redshift $z = 0$ snapshot of a parent dark matter only simulation with a comoving side length of 100 cMpc from the EAGLE project (L100N1504) introduced in Schaye et al. (2015). Initial conditions for the zoom re-simulations of the selected haloes were created at $z = 127$, using the procedure outlined in Jenkins (2010) and assuming the Planck Collaboration XVI (2014) cosmological parameters: $\Omega_m = 0.307$, $\Omega_b = 0.048$, $\Omega_\Lambda = 0.693$, and a Hubble constant of $H_0 = 100h$ km s^{-1} Mpc^{-1}, where $h = 0.6777$. The haloes are then re-simulated with full baryonic physics with higher resolution around the main halo.

The simulations were performed with the magneto-hydrodynamic code AREPO (Springel 2010) and a comprehensive galaxy formation model (see Vogelsberger et al. 2013; Marinacci et al. 2014; Grand et al. 2017, for more details). This model includes atomic and metal line cooling (Vogelsberger et al. 2013) and a spatially uniform UV background (Faucher-Giguère et al. 2009), which fully re-ionizes hydrogen at redshift 6. A subgrid model for the interstellar medium and star formation (Springel & Hernquist 2003) is employed. Stellar evolution is treated self-consistently and includes metal enrichment from core collapse supernovae, thermonuclear supernovae, and asymptotic giant branch stars (Vogelsberger et al. 2013). Feedback from core collapse supernovae is taken into account through a non-local effective wind model that isotropically carries thermal and kinetic energy in equal partition away from the star-forming ISM. The winds are hydrodynamically decoupled from the gas until they encounter gas with a density below 10 per cent of the star formation threshold, at which time they are re-coupled to the gas. As a result, the winds deposit mass, metals, and energy and impart momentum predominantly to gas that surrounds the star-forming regions. The metal content of the winds is equal to $1 - \eta$ times the total mass of metals of the star-forming gas from which they are launched, where $\eta = 0.6$. The rate at which winds are launched is determined by the mass-loading factor, which depends on the energy available for supernovae (given by the star formation rate) and the wind velocity, which we set equal to 3.46 times the local 1D dark matter velocity dispersion (Okamoto et al. 2010).

Star particles are assumed to be simple stellar populations (SSPs) and are assigned broad-band luminosities based on the catalogues of Bruzual & Charlot (2003). Stellar mass-loss and metal enrichment are modelled by calculating at each time-step the mass (and metal content thereof) moving off the main sequence for each star particle according to a Chabrier (Chabrier 2003) initial mass function (IMF), which is then distributed isotropically into surrounding gas cells. Lower and upper mass limits of 0.1 and 100 $M_\odot$, respectively, are set for the integration limits. The mass and metals are then distributed among nearby gas cells with a top-hat kernel. We track a total of nine elements: H, He, C, O, N, Ne, Mg, Si, and Fe.

The model further includes the seeding, growth, and feedback from supermassive black holes (Springel et al. 2005). The gas accretion rate is given by the Bondi–Hoyle–Lyttleton model (Bondi & Hoyle 1944; Bondi 1952, BHL hereafter), and a term designed to balance the energy lost from the intracluster medium of the halo in the form of X-ray emission is based on the model of Nulsen & Fabian (2000, hereafter NF). The BHL accretion rate gives rise to thermal energy feedback injected into surrounding gas cells, whereas the NF term provides thermal energy required to inflate small bubbles of hot gas in the halo in a smooth fashion.

Magnetic fields are included in the limit of ideal magnetohydrodynamics, which is described in detail in Pakmor & Springel (2013) and Pakmor et al. (2017). A uniform magnetic seed field with comoving strength, 10^{-14} G, is set at $z = 127$ (equal to a physical strength of $2 \times 10^{-4}\mu$G) oriented along the z-coordinate of the simulation cube. We note that although this seed field strength is many orders of magnitudes larger than plausible values for a cosmological seed field from inflation or fields seeded by Biermann batteries (Kulsrud & Zweibel 2008), the information about the initial configuration and strength of the magnetic field is quickly erased by an exponential dynamo in collapsed haloes (Pakmor et al. 2014; Marinacci et al. 2015). The initial strength is sufficiently small to be dynamically irrelevant outside collapsed haloes (Marinacci & Vogelsberger 2016).

In this paper, we focus on the highest resolution simulations of the AURIGA suite, which correspond to the 'level 3' resolution described in Grand et al. (2017). The galaxies were selected to have large discs (Au 16, Au 24), to be close analogues of the Milky Way as measured, for example, by stellar mass, star formation rate, and morphology (Au 6), or for interesting satellite interactions (Au 21, Au 23, Au 27). The typical dark matter particle mass is $\sim 4 \times 10^4$ $M_\odot$, and the baryonic mass resolution is $\sim 5 \times 10^3$ $M_\odot$. The physical softening of collisionless particles increases with time up to a maximum physical softening length of 185 pc, which is reached at redshift 1. The physical softening value for the gas cells is scaled by the gas cell radius (assuming a spherical cell shape given the volume), with a minimum softening set to that of the collisionless particles.

Final face-on and edge-on stellar luminosity images for these systems are shown in Fig. 1. We list some relevant properties of the simulations in Table 1. The disc scale lengths, derived from fits to the surface density distribution of stars $\leq$1 kpc of the mid-plane, range from 3.2 to 6.1 kpc, and implied stellar disc masses from 2.6×10^{10} to 5×10^{10} $M_\odot$, which are similar to current estimates for the Milky Way (Bland-Hawthorn & Gerhard 2016). We remark that each of the simulated discs can be decomposed into a thick and thin disc at $R \sim 8$ kpc (see Fig. 2 and Table 1) with scale height values similar to those of the Milky Way. The simulated

[1] Defined to be the mass inside a sphere in which the mean matter density is 200 times the critical density, $\rho_{\rm crit} = 3H^2(z)/(8\pi G)$.

[2] The centre of a target halo must be located outside nine times the R_{200} of any other halo that has a mass greater than 3 per cent of the target halo mass.

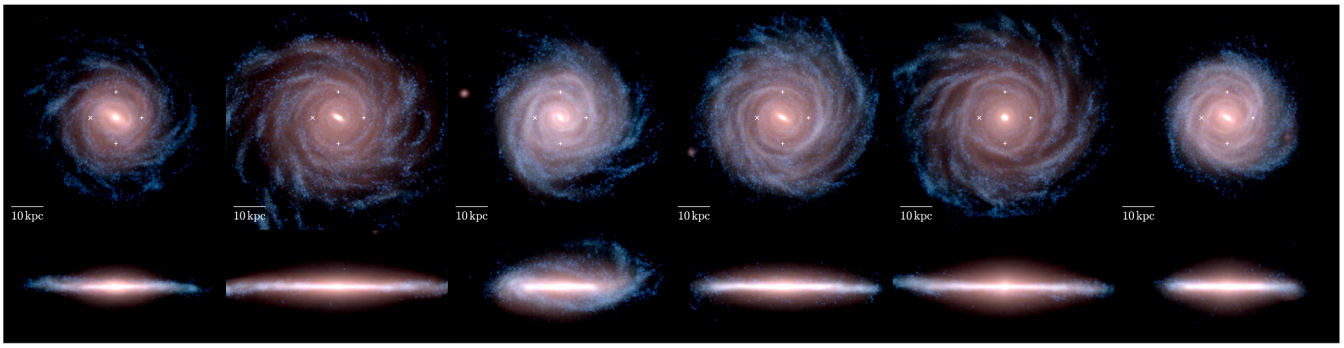

Figure 1. Face-on and edge-on projected stellar densities at $z = 0$ for the six high-resolution simulations from which we construct mock catalogues. The images are a projection of the *K*-, *B*- and *U*-band luminosity of stars, shown by the red, green, and blue colour channels, in logarithmic intervals, respectively. Younger (older) star particles are therefore represented by the bluer (redder) colours. The box side-length is 70 kpc in each panel. The cross in each panel (leftmost white symbol) indicates the default solar position, whereas the plusses indicate the other choices. Movies and images are available at http://auriga.h-its.org.

Table 1. Table of properties of each simulation. The columns are (1) halo number, (2) virial mass, (3) virial radius, (4) stellar mass within the virial radius, (5) stellar disc mass calculated as $2\pi\Sigma_0 R_{\rm d}^2$, where Σ_0 and $R_{\rm d}$ are the parameters retrieved from a bulge-disc surface density decomposition performed in the same way as in Grand et al. (2017) for the mass within 1 kpc of the disc mid-plane, (6) stellar disc scale length, (7) circular rotation velocity at a radius of 8 kpc, calculated as $V_{\rm c} = \sqrt{GM(<R = 8\,{\rm kpc})/8\,{\rm kpc}}$, (8) azimuthally averaged stellar surface density within 1 kpc of the mid-plane at $R = 8$ kpc, 9) thin and thick (bracketed values) disc scale heights of a double sech^2 decomposition of the vertical density distribution in a 1 kpc-wide annulus centred at $R = 8$ kpc (see Fig. 2) and (10) vertical velocity dispersion of stars within 1 kpc of the disc mid-plane at $R = 8$ kpc. The last row provides current estimates of all of these quantities for the Milky Way. All values are taken directly from Bland-Hawthorn & Gerhard (2016). †The mean of values for R_{200} provided in table 8 of that paper, the standard deviation of which is 28.6. ‡Observationally derived vertical scale height and velocity dispersion of the old thin disc and thick disc (bracketed values) at the solar neighbourhood.

Run	$\frac{M_{\rm vir}}{(10^{12}{\rm M}_\odot)}$	$\frac{R_{\rm vir}}{({\rm kpc})}$	$\frac{M_*}{(10^{10}{\rm M}_\odot)}$	$\frac{M_{*,{\rm d}}}{(10^{10}\,{\rm M}_\odot)}$	$\frac{R_{\rm d}}{({\rm kpc})}$	$\frac{V_{\rm c}\,(R_\odot)}{({\rm km\,s^{-1}})}$	$\frac{\Sigma\,(R_\odot)}{({\rm M}_\odot\,{\rm pc}^{-2})}$	$\frac{h_z\,(R_\odot)}{({\rm pc})}$	$\frac{\sigma_z\,(R_\odot)}{({\rm km\,s^{-1}})}$
Au 6	1.01	211.8	6.1	2.6	3.3	224.7	33.2	339 (1139)	39.8
Au 16	1.50	241.5	7.9	3.7	6.0	217.5	44.5	303 (1130)	40.2
Au 21	1.42	236.7	8.2	3.8	3.3	231.7	51.8	430 (1363)	44.0
Au 23	1.50	241.5	8.3	4.0	5.3	240.0	52.5	339 (1260)	42.0
Au 24	1.47	239.6	7.8	2.8	6.1	219.2	31.5	330 (1436)	42.4
Au 27	1.70	251.4	9.5	5.0	3.2	254.5	71.1	302 (1103)	42.1
MW	1.3 ± 0.3	†220.7	6 ± 1	4 ± 1	2.6 ± 0.5	238 ± 15	33.3 ± 3	‡300 ± 50 (900 ± 180)	‡25 ± 5 (50 ± 5)

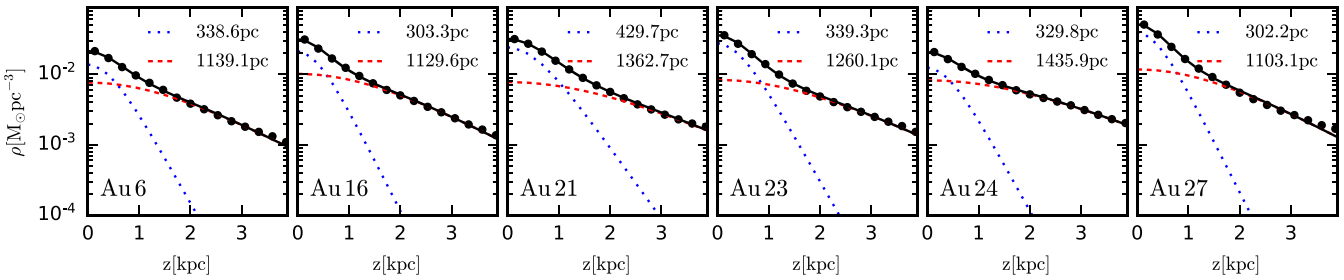

Figure 2. Profiles of the stellar vertical density distribution in a 1 kpc-wide annulus centred at $R = 8$ kpc, for each simulation. A double sech^2 profile is fitted (black curves) to the raw density distribution (black circles). The profile is composed of a thin (blue dotted curves) and a thick (red dashed curves) disc, the scale heights of which are denoted in each panel. In each case, values similar to the Milky Way values are obtained (see Table 1).

vertical velocity dispersion is calculated from all stars within 1 kpc of the disc mid-plane at $R \sim 8$ kpc and falls between the thin and thick disc values derived observationally. (e.g. McMillan 2011). The ability of these simulations to produce coherent, radially extended discs with barred and spiral structure and stellar haloes from a self-consistent cosmological galaxy formation model from ΛCDM initial conditions makes these simulations powerful predictors for the formation of galaxies such as the Milky Way. In the next section, we describe how we generate the mock *Gaia* catalogues from the simulations.

3 MOCK STELLAR CATALOGUES

The first step to create a mock stellar catalogue is to choose the position and velocity of the Sun. For each simulation, we define four choices for the solar position: all adopt a radius and height above

the mid-plane (defined at redshift 0) of $(R_\odot, Z_\odot) = (80.02)$ kpc, and are spread at equidistant azimuthal angles relative to our default reference angle, which is chosen to be 30 deg behind[3] the major axis of the bar (Bland-Hawthorn & Gerhard 2016) The bar major axis is calculated from the $m = 2$ Fourier mode of the central 5 kpc stellar distribution (see Grand, Kawata & Cropper 2013, for details on how to extract angles from modes). We then rotate the disc such that the solar position is placed at the Galactocentric Cartesian coordinate $(X, Y, Z) = (-R_\odot, 0, Z_\odot)$. We set the local standard of rest equal to the spherically averaged circular velocity at the solar radius, and set the solar motion velocity to $(U_\odot, V_\odot, W_\odot) = (11.1, 12.24, 7.25)$ km s^{-1} (Schönrich, Binney & Dehnen 2010) relative to the local standard of rest. After setting the solar position and velocities, we transform our coordinate system to heliocentric equatorial coordinates following the matrix transformation described in section 3 of Hunt & Kawata (2014), and we retain this coordinate system in the mock catalogue output.

For each of the four solar positions, we generate two sets of mock catalogues: one set is generated by a parallelized version of SNAPDRAGONS[4] (Hunt et al. 2015; HITS-MOCKS); the other set is generated using the method presented in Lowing et al. (2015; ICC-MOCKS), who produced SDSS mocks based on the Cooper et al. (2010) particle tagging technique applied to the AQUARIUS simulations (Springel et al. 2008). Mateu et al. (2017) added *Gaia* observables to the Lowing et al. (2015) mocks to make predictions for the detection of tidal streams in *Gaia* data using great-circle methods.

Both methods assume that each simulation star particle is an SSP that can be transformed into individual stars by sampling from a theoretical isochrone matching the particle's age and metallicity. They compute observable properties of stars and their associated errors in the same way and apply identical selection functions. The methods differ in how the stars are distributed in phase space and their choice of stellar evolution models. The step-by-step procedure for generating each set of catalogues is as follows:

HITS-MOCKS

(i) apply a stellar population synthesis model to each star particle;
(ii) add dust extinction;
(iii) apply the observational selection based on a magnitude cut;
(iv) convolve observable properties with *Gaia* DR2 errors and displace stellar coordinates.

ICC-MOCKS

(i) apply a stellar population synthesis model to each star particle;
(ii) add dust extinction;
(iii) distribute individual stars over the approximate phase-space volume of the parent star particle;
(iv) apply the observational selection based on a magnitude cut;
(v) convolve observable properties with *Gaia* DR2 errors and displace stellar coordinates.

We note that the HITS-MOCKS displace stars from their parent particles (true coordinates) to their observed coordinates by random sampling the DR2 error distributions for astrometry and radial velocity of the mock star. However, the ICC-MOCKS distribute stars over a 6D kernel approximating the phase-space volume of their parent particle, which become the true coordinates, and are afterwards displaced to their observed coordinates by error sampling in the same way as the HITS-MOCKS. In addition, we generate a version of the ICC-MOCKS without extinction by omitting step (ii), which we denote as ICC-MOCKS-NOEX. We discuss the advantages and disadvantages of this choice below, where we describe each stage in detail.

3.1 Stellar population synthesis

The basic premise of the population synthesis calculation in both the HITS-MOCKS and ICC-MOCKS is that each simulation star particle corresponds to an SSP with an evolutionary state defined by a single metallicity and age and a total number of stars proportional to its mass. The present-day mass distribution of individual stars in the SSP is determined by the convolution of an assumed IMF by a model of stellar evolution (encapsulated in a set of pre-computed isochrones), which takes into account processes such as the death of massive stars and mass-loss from those that survive.

For the HITS-MOCKS, although the simulations use a Chabrier IMF, SNAPDRAGONS only contains implementations of the Salpeter (Salpeter 1955) and Kroupa (Kroupa 2001) IMFs. Thus, we use a Kroupa IMF to sample the distribution of present-day stellar masses for each SSP that is the closer approximation of the Chabrier IMF used in the AURIGA simulations. We set the minimum allowed initial stellar mass to be 0.1 $M_\odot$ (as for the AURIGA simulations). For a given SSP, we set the lower mass limit to be the lowest present-day stellar mass that would be visible at our limiting magnitude (see next), and the upper stellar mass limit to be the maximum stellar mass that would still be present at the age of our model particle. We then integrate the IMF over the desired mass range to determine the number of stars that would be visible within this mass range, N_s, and randomly sample the IMF N_s times. Note that while we do not generate any stars below the visible limit, we do account for their mass. The process is discussed in more detail in Hunt et al. (2015).

The procedure described above is similar for the ICC-MOCKS, which use a Chabrier IMF. To sample the SSP, we choose small intervals of initial mass in the range[5] 0.08–120 $M_\odot$. Given the total initial mass of the SSP, we calculate the expected number of stars in each interval. Finally, the actual number of stars in each mass interval is randomly generated from a Poisson distribution with the corresponding expectation value.

Once, we have sampled the stellar mass distribution for a given star particle, we are in a position to assign stellar parameters such as temperature, magnitudes, and colours to each synthetic star. For the ICC-MOCKS, we use the PARSEC isochrones (Bressan et al. 2012; Chen et al. 2014, 2015; Tang et al. 2014). These represent up-to-date stellar models that span a wide range of metallicities and ages and have magnitudes in multiple bands, including the *Gaia* ones. We downloaded isochrone tables from the `CMD v3.0` web interface[6] using the default options. We sample a grid of isochrones

[3] *Behind* means an angle measured from the bar major axis in the direction opposite to that of the rotation of the Galactic disc. We note that an effectively random azimuthal position is chosen for Au 24, which does not have a bar.
[4] Serial version available at https://github.com/JASHunt/Snapdragons.

[5] We note that the lower mass limit of 0.08 is lower than the limit of 0.1 adopted by the AURIGA simulations, however, M7V–M8V stars of this mass have an absolute V −band magnitude of ∼18 (fainter than our $V < 16$ allsky sample) and an apparent magnitude fainter than $V = 20$ at distances farther than 25 pc from the Sun (with no extinction). These extremely faint stars will therefore not be observed for the vast majority of applications. The upper mass limit of 120 $M_\odot$ is higher than the 100 $M_\odot$ assumed in AURIGA; however, such massive stars are extremely rare therefore we do not expect them to bias any results.
[6] http://stev.oapd.inaf.it/cgi-bin/cmd_3.0

spanning the age range $6.63 \leq \log(t/\mathrm{yr}) \leq 10.13$, with a step size, $\Delta \log(t/\mathrm{yr}) = 0.0125$, and the metallicity range $0.0001 \leq Z \leq 0.06$. Because interpolating between pre-computed isochrones is non-trivial, we identify the isochrone with the closest value in age and metallicity for each star particle. Any of the particles that lie outside the range of the age/metallicity grid are also matched to the nearest isochrone.

For the HITS-MOCKS, we use the same procedure as described above but use an earlier version of the PARSEC isochrones (Marigo et al. 2008), which are currently used in the SNAPDRAGONS code. This set of isochrones uses a slightly different range of ages and metallicities for the grid compared to those used for the ICC-MOCKS: $6.6 \leq \log(t/\mathrm{yr}) \leq 10.22$, with a step size, $\Delta \log(t/\mathrm{yr}) = 0.02$ and $0.0001 \leq Z \leq 0.03$. We do not expect that the properties of most stellar populations in our catalogues will be significantly affected by the differences between these two sets of isochrones.

3.2 Dust extinction

Dust extinction can be problematic for Galactic optical surveys, such as *Gaia*, mainly because of the poorly understood 3D distribution of dust in the Milky Way. As an approximation, the HITS-MOCKS use the extinction maps used in GALAXIA (Sharma et al. 2011), based on the method presented in Bland-Hawthorn, Krumholz & Freeman (2010) to derive a 3D polar logarithmic grid of the dust extinction generated from the 2D dust maps of Schlegel, Finkbeiner & Davis (1998) and the assumption of a uniform distribution of dust along a given line of sight. From these maps, we calculate a magnitude extinction for each magnitude band and, given the distance modulus for the original star particle, we determine the apparent magnitude in each band.

We note that the alternative philosophy of modelling dust directly from the gas and dust distribution in the simulations will make the dust map more consistent with large-scale features of the AURIGA galaxies (such as spiral arms). However, going beyond uncertain, simplistic dust models based solely on the metallicity of simulation gas cells is far from straightforward (e.g. Trayford et al. 2017). On the other hand, the use of a dust map based on the Milky Way results in one fewer discrepancy between the mock catalogues and observations that use the same dust maps; this may facilitate their intercomparison because the selection function will be more consistent with *Gaia*.

The ICC-MOCKS-NOEX do not include dust extinction, and hence the user is free to adjust magnitudes for extinction themselves, if required. We note also that dust extinction is less important for stellar halo studies, which typically exclude high extinction regions in the Galactic mid-plane.

3.3 Phase-space sampling

This step is applied only to the ICC-MOCKS. Once we have generated a catalogue of stars, the ICC-MOCKS method assigns distinct positions in configuration and velocity space to each of them. The intention of this step, which can be thought of as a form of smoothing, is to avoid discrete 'clumps' of stars at the coordinates of the parent particles. We follow the implementation of Lowing et al. (2015), which is similar to that introduced by the GALAXIA code (Sharma et al. 2011). For every simulation particle, we construct a 6D hyper-ellipsoidal 'smoothing kernel' that approximates the volume of phase space the particle represents. We distribute the stars associated with particles into these 6D kernels as described next. In this way, we approximately preserve coherent phase-space structures in the original simulation, such as tidal streams (e.g. in configuration space, this approach ensures stars are displaced more along such streams than they are perpendicular to them). It is important to note that, although the resulting distribution of stars represents a denser sampling of phase space, it is essentially an interpolation (and extrapolation, around the edges of the phase space of the simulation). It does not add any (physical) dynamical information or increase the resolution beyond that of the parent simulation.

The phase-space volume associated with each star particle is estimated using the ENBID code of Sharma & Steinmetz (2006). This code numerically estimates the 6D phase-space density around each particle using an entropy based criterion to partition the set of particles into a binary tree, without the need to specify a metric-relating configuration and velocity space. The resulting estimate of the phase-space volume of each leaf node can be noisy due to Poisson sampling, so we further apply an anisotropic smoothing kernel. We use the nearest 64 neighbours to locally determine the principal directions and to locally re-scale the phase space. In this rotated and re-scaled phase space, we define the phase-space volume, $V_{6\mathrm{D}}$, of each star particle as 1/40 of the hypersphere that encloses the nearest 40 neighbours. The actual phase-space sampling kernel is a 6D isotropic Gaussian with zero mean and dispersion, $\sigma^2 = \gamma R_{6\mathrm{D}}^2$, where $\gamma = 1/48$ and $R_{6\mathrm{D}}$ is the radius of the hypersphere with volume, $V_{6\mathrm{D}}$. To avoid extreme outliers in the Gaussian tails of these kernels, we truncate the kernels at 5σ. We draw coordinates randomly from the kernel defined by each parent star particle for each star it generates. Each randomly generated point is then transformed back from this rotated and re-scaled phase space into the Cartesian configuration and velocity space of the original simulation. We call these new coordinates the 'true' coordinates. This definition differs from that in the HITS-MOCKS, in which the 'true' positions correspond to those of the parent star particle. See Lowing et al. (2015) for a more detailed description and several tests of the phase-space sampling method.

To avoid unnecessary oversmoothing due to 'cross-talk' between different phase-space structures, we partition the stellar particles into sets according to their progenitor galaxy and calculate the scale of the phase-space kernels for a given particle using only neighbours from the same set. For this purpose, we use the AURIGA merger trees built from SUBFIND groups (Grand et al. 2017). We trace back each stellar particle to the first snapshot in which it belonged to the same FOF halo as the main progenitor of the Milky Way halo analogue. Particles that did not form '*in situ*' in the central galaxy are grouped according to their subfind group membership at the snapshot immediately prior to this (i.e. just before their first infall into the main progenitor halo). We assign all particles that did form in the central galaxy to a single group (we discuss a potential limitation of this implementation in Section 5.1). Again, further details are given in Lowing et al. (2015).

3.4 Mock survey selection function

In order to limit the size of our mock catalogues to the order of $\sim 10^8$ stars instead of $\gtrsim 10^9$ stars, we provide a full sky catalogue only for stars with $V < 16$. Most stellar halo stars are fainter than this, so to have a large sample of stars for stellar halo science we supplement this bright star catalogue by including stars with $16 < V < 20$ for Galactic latitudes $|b| > 20$ deg. These selection cuts are applied to both the HITS-MOCKS and the ICC-MOCKS.

We note that in the HITS-MOCKS, faint stars are randomly sampled at a rate of 20 per cent in order to reduce the output size. However,

this does not bias data trends aside from the number of stars available in the magnitude range $16 < V < 20$.

3.5 *Gaia* DR2 errors

In this subsection, we describe how we add *Gaia* DR2 errors to the catalogues, which is the same for both the HITS-MOCKS and ICC-MOCKS. We convolve the parameters of the selected stars with *Gaia*-like errors as a function of magnitude and colour in the Johnson-Cousins V and I_c bands following Jordi et al. (2010):

$$G = V - 0.0257 - 0.0924(V - I_c) - 0.1623(V - I_c)^2 + 0.009(V - I_c)^3. \quad (1)$$

We use the post-launch error estimates approximated from the estimates in pre-launch provided through the Gaia Challenge collaboration performance (Romero-Gómez et al. 2015), which include all known instrumental effects such as stray light levels and residual calibration errors. A simple performance model that takes into account the wavelength dependence of the point spread function and reproduces the end-of-mission parallax standard error estimates is

$$\sigma_{\pi_{\rm final}}[\mu{\rm as}] = (-1.631 + 680.766z + 32.732z^2)^{0.5} \times [0.986 + (1 - 0.986)(V - I_c)], \quad (2)$$

where

$$z = \max\left(10^{0.4(12.09-15)}, 10^{0.4(G-15)}\right), \quad (3)$$

and $6 \leq G \leq 20$ denotes the range in broad-band, white-light, *Gaia* magnitudes. This relation reflects the magnitude-dependent errors for stars observed by *Gaia*. Stars in the range $6 \leq G \leq 12$ will have shorter integration times in order to avoid CCD saturation and are assigned a constant $\sigma_\pi = 7$ μas error by the above relation.

The basic mission results improve with increasing mission time, t, as $t^{-0.5}$ for the positions, parallaxes, photometry, and radial velocities and $t^{-1.5}$ for the proper motions.[7] Given that these errors are end-of-mission estimates, we adopt the following simple scaling to provide the expected parallax-standard error for DR2:

$$\sigma_\pi = L\sigma_{\pi_{\rm final}}, \quad (4)$$

where $L = (60/22)^{1/2}$, which corresponds to the square root of the DR2 mission time divided by the total 5 yr mission time. The right ascension, declination, and proper motions are all scaled with this factor as well.

The errors in position on the sky (α, δ) and proper motions (μ_α, μ_δ) scale with the ecliptic longitude averaged error of the sky-varying factors derived from scanning law simulations, the values of which are listed on the *Gaia* performance website.[8]

DR2 will provide radial velocities for only a very small subset of stars near the Sun with spectral type later than F. However, the selection function and error function is non-trivial, involving, for example, the number of visits, binarity, and temperature. Thus, we provide estimates of the radial velocity error for all generated stars, using the end of mission *Gaia* error that adopts the simple performance model:

$$\sigma_{v_r} = 1 + be^{a(V-12.7)}, \quad (5)$$

where a and b are constants that depend on the spectral type of the star. We caution the reader that the radial velocities are both more plentiful and more accurate than the expected DR2 radial velocities.

In addition to astrometric errors, we calculate the red and blue broad-band *Gaia* magnitudes, $G_{\rm RP}$ and $G_{\rm BP}$, and errors for all *Gaia* photometric bands, according to the single-field-of-view-transit standard error on the *Gaia* science performance website, modified to include the DR2 mission time scaling and 20 per cent calibration errors:

$$\sigma_{\rm G} = 5\frac{1.2 \times 10^{-3}L}{\sqrt{70}} \times \left(0.04895z^2 + 1.8633z + 0.0001985\right)^{1/2}, \quad (6)$$

and

$$\sigma_{G_{\rm RP/BP}} = 5\frac{1 \times 10^{-3}L}{\sqrt{70}} \times \left(10^{a_{\rm BP/RP}}z^2 + 10^{b_{\rm BP/RP}}z + 10^{c_{\rm BP/RP}}\right)^{1/2}, \quad (7)$$

where $a_{\rm BP/RP}$, $b_{\rm BP/RP}$, and $c_{\rm BP/RP}$ are listed on the *Gaia* science performance website. We note that the factor of 5 in the pre-factor of equations (6) and (7) is required to scale the photometric errors to match the ∼ millimag accuracy at the bright end ($G < 13$ mag) and the 20 and 200 millimag accuracy at the faint end for G and $G_{\rm RP/BP}$, respectively, that are quoted on the *Gaia* DR2 website.

We provide error estimates for atmospheric parameters based on the results of Liu et al. (2012), who inferred the expected performance of stellar parametrization from various fitting methods applied to synthetic spectra. Specifically, a second-order polynomial in G has been fitted to the mean-averaged residual of effective temperature and surface gravity inferred from the Bayesian method Aeneas (Bailer-Jones 2011).

For both the HITS-MOCKS and the ICC-MOCKS, we randomly sample these standard errors for each generated mock star (which satisfies our magnitude cut) to displace the measured parallax, proper motions, and radial velocity of each synthetic star from that of its parent particle. This ensures that, for the reasons discussed in Section 3.3, the position and velocity coordinates of each star are distinct from those of their parent star particle in the case of the HITS-MOCKS. The standard errors for the *Gaia* photometric bands (equations 6 and 7) and effective temperatures are randomly sampled and added to the true values to produce observed values for these quantities.

3.6 Access to mock catalogues

The HITS-MOCKS and ICC-MOCKS presented in this paper will be made available to the community upon submission of this article. They will be available to download from the AURIGA website[9] as well as the Virgo Millennium database in Durham,[10] which also allows subsets of data to be retrieved using SQL queries. In addition, snapshot particle data and gravitational potential grids will be made available at these locations. A description of the data fields and their units is given in Table A1.

4 THE MOCK CATALOGUES AND EXAMPLE APPLICATIONS

Fig. 3 shows all-sky maps of the observed mock stellar distributions in heliocentric equatorial coordinates (right ascension and declination) for one of the HITS-MOCKS. These maps are constructed by

[7] http://www.astro.lu.se/gaia2017/slides/Brown.pdf
[8] https://www.cosmos.esa.int/web/gaia/science-performance
[9] http://auriga.h-its.org
[10] See http://icc.dur.ac.uk/data

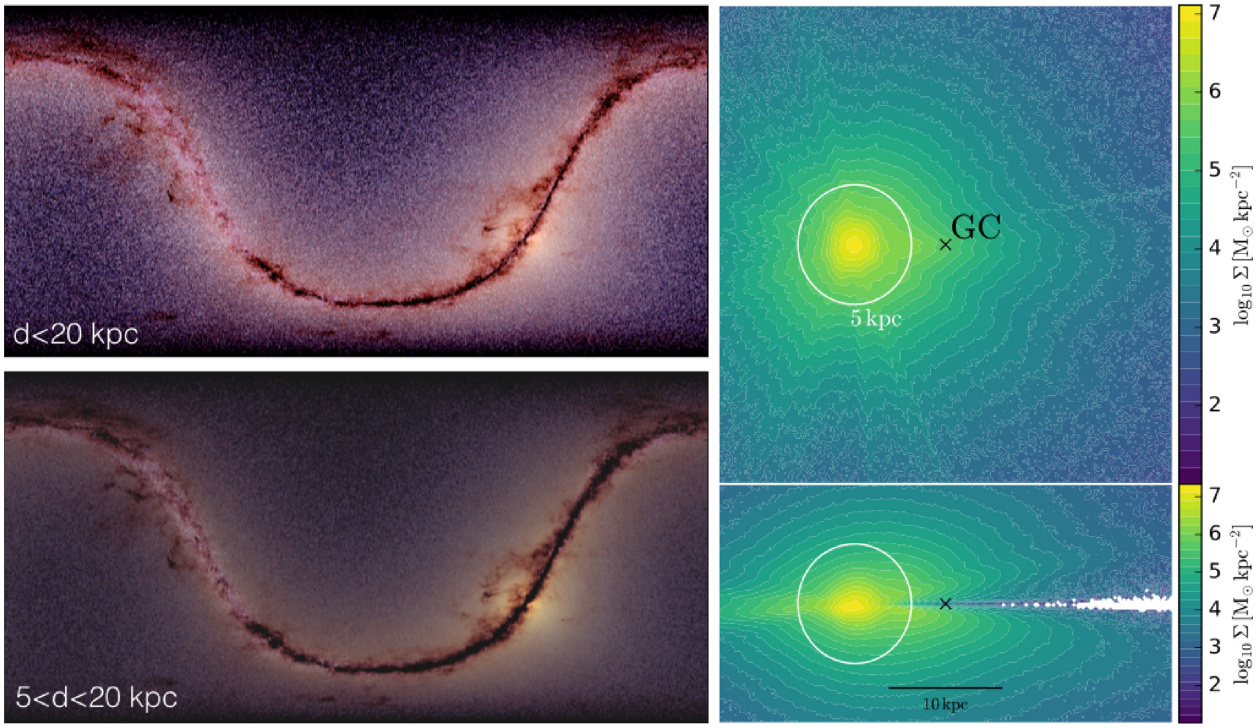

Figure 3. *Left:* Three-colour all-sky maps in heliocentric equatorial coordinates of the default HITS-MOCK for Au 24. These maps are constructed from mapping the *K*-, *G*-, and *U*-band apparent magnitudes to the red, green, and blue colour channels of the composite image. The *x* and *y* axes represent right ascension (RA) and declination (Dec.), respectively. The upper image shows the stellar light distribution for all stars up to a 20 kpc heliocentric distance, *d*, whereas the lower image shows the map for stars between 5 and 20 kpc heliocentric distance. *Right:* Contour maps show the projected face-on (top panel) and edge-on (bottom panel) stellar mass surface density, respectively, with annotations for the Galactic Centre and 5 kpc heliocentric distance, to guide the eye.

mapping the *K*-, *G*-, and *U*-band apparent magnitudes of stars to the red, green, and blue colour channels of the composite image. The upper all-sky map includes all stars out to 20 kpc heliocentric distance and clearly shows the presence of a central yellow bulge and blue disc. The blue light from nearby stars extends above the Galactic mid-plane and fades with increasing latitude. Immediately obvious is the dust obscuration in the disc mid-plane, which coincides with the disc plane and is pronounced in directions towards the bulge. In the lower all-sky map, we show all stars within 5–20 kpc distance. In this volume, the bulge and outer disc are emphasised because stars that make up these components contribute more to the map than the local disc. In turn, dust obscuration is more obvious. For clarity, Fig. 3 also shows the surface mass density of the mock stellar distribution in Cartesian coordinates (face-on: top-right panel; edge-on: bottom-right panel). We note that the observed distribution of stars is more extended than the true distribution because the *Gaia* DR2 errors can become large at large distances, which for the HITS-MOCKS translate to large displacements of stars in phase space and thus to an inevitable increase in the observed phase-space domain.

Fig. 4 shows the apparent *G*-magnitude distribution of stars in each of the HITS-MOCKS (top panel) and ICC-MOCKS-NOEX (bottom panel) generated from the default solar position (30 deg behind the bar major axis). We reiterate that catalogues cover the full sky for stars with magnitudes $V < 16$, whereas fainter stars with $16 < V < 20$ are only provided at latitudes $|b| > 20$ deg. The lower number of stars fainter than $V = 16$ reflects the 20 per cent sampling rate of these stars in the HITS-MOCKS. These distributions do not vary significantly between the mock catalogues. We note that the *G*-magnitude distributions for the ICC-MOCKS are very similar to those of the HITS-MOCKS therefore for brevity we omit the former.

In the first two panels of Fig. 5, we show the HITS-MOCK and ICC-MOCK colour–magnitude diagram (CMD) for Au 24 at the default solar position. Following Gaia Collaboration (2018d), we selected stars with parallax errors better than 10 per cent; *G* magnitude errors better than 0.22 mag; $G_{BP/RP}$ magnitudes better than 0.054 mag. These CMDs contain the full spectral range of main-sequence stars and feature prominent evolutionary stages such as the main-sequence turn-off and the red giant branch. The corresponding CMD of the ICC-MOCKS-NOEX is shown in the third panel of Fig. 5 and clearly illustrates the effects of reddening and extinction on comparison with the second panel: the main sequence and turn-off are much sharper and bluer in the absence of dust. In the fourth panel of Fig. 5, we impose an additional selection criterion for stars with little extinction ($A_0 < 0.03$) for the ICC-MOCK. This enhances the clarity of the CMD features (compared to the second panel) and demonstrates that our CMDs are qualitatively similar to those presented in Gaia Collaboration (2018d). We note that we do not model the white dwarf sequence, which is the main difference between these simulated CMDs and *Gaia* CMDs.

In the remainder of this section, we present applications of the mock data to the stellar disc and halo. We restrict ourselves to two applications, the flaring (young) stellar disc and the stellar halo spin.

4.1 Flaring disc(s)

In the last years, both simulations and observations have increasingly focused on the chemical and age structure of the stellar disc (e.g. Schönrich & Binney 2009; Bovy, Rix & Hogg 2012; Rahimi,

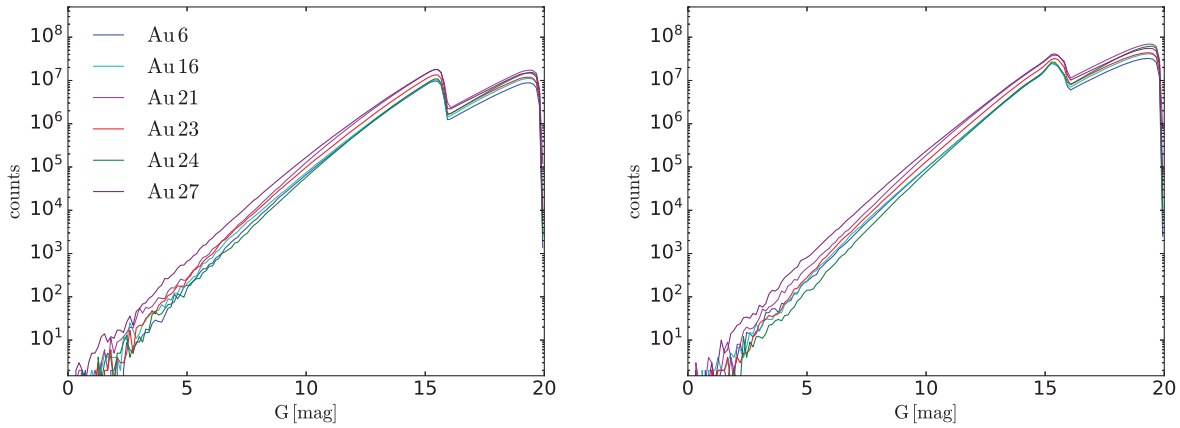

Figure 4. The distribution of stars as a function of G-magnitude in the HITS-MOCKS (left-hand panel) and the ICC-MOCKS-NOEX (right-hand panel) for the default solar position of each simulation. The step at $V \sim 16$ reflects our choice to select stars with $16 < V < 20$ at latitudes $|b| > 20$ deg, whereas the stars brighter than $V = 16$ are sampled with full sky coverage. The bin size is 0.1 mag.

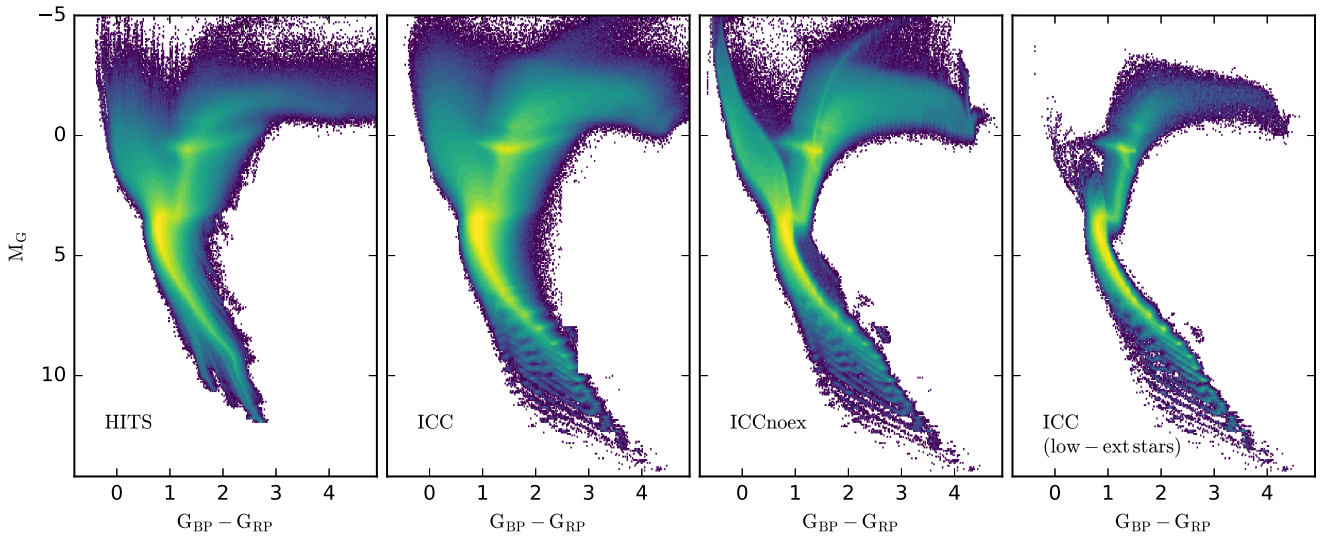

Figure 5. *Gaia* CMDs for mock catalogues generated for Au 24 at the default solar position. These are constructed by sampling the stellar particles taking into account the mass, age, and metallicity of each particle according to the corresponding IMF. The first three panels show a HITS-MOCK, ICC-MOCK and ICC-MOCK-NOEX for a subset of stars with accurate astrometry and photometry (see text for detailed selection criteria). The fourth panel shows the same as the second panel but with an extra selection cut for stars with low extinction.

Carrell & Kawata 2014; Minchev, Chiappini & Martig 2014a; Hayden et al. 2015; Mackereth et al. 2017; Schönrich & McMillan 2017). An interesting result of these analyses is that the outer disc of the Milky Way is composed of subpopulations of age (and metallicity), each of which flare.[11] This sort of flaring distribution is often seen in numerical simulations that include orbiting satellites and mergers (e.g. Quinn, Hernquist & Fullagar 1993; Martig, Minchev & Flynn 2014; Minchev et al. 2014b) that act to preferentially dynamically heat the outer disc more than the inner disc. However, an alternative, internal mechanism that may give rise to disc flaring is the radial migration of stars from the inner disc to the outer disc: Bovy et al. (2016) has shown that the degree of flaring found in the APOGEE red clump data is consistent with theoretical predictions of the radial migration of stars under conservation of vertical action arguments (Minchev et al. 2012; Solway, Sellwood & Schönrich 2012; Roškar, Debattista & Loebman 2013). This finding suggests a secular dynamical origin for the flared distributions; however, the origin remains to be conclusively determined and is still debated.

Although much attention has been paid to dynamical origins, there is growing evidence that the flared distributions may be formed *in situ* from flaring star-forming regions. Grand et al. (2016) showed that a significant amount of the vertical velocity dispersion is set at birth from star-forming gas that becomes progressively thinner with time and that, at a given look back time, the radial profile of the vertical velocity dispersion of young stars (<1 Gyr old) is flat, corresponding to a flaring scale height. Navarro et al. (2018) showed from the Apostle simulations (Sawala et al. 2015; Fattahi et al. 2016) that stars are born in flared distributions. Moreover, these distributions do not change significantly thereafter; they are not strongly affected by subsequent dynamical processes. This idea that the star-forming gas disc intrinsically flares is supported also by the simple analytical arguments put forward by Benítez-Llambay

[11] The term *flare* refers to an increase in scale height with increasing radius.

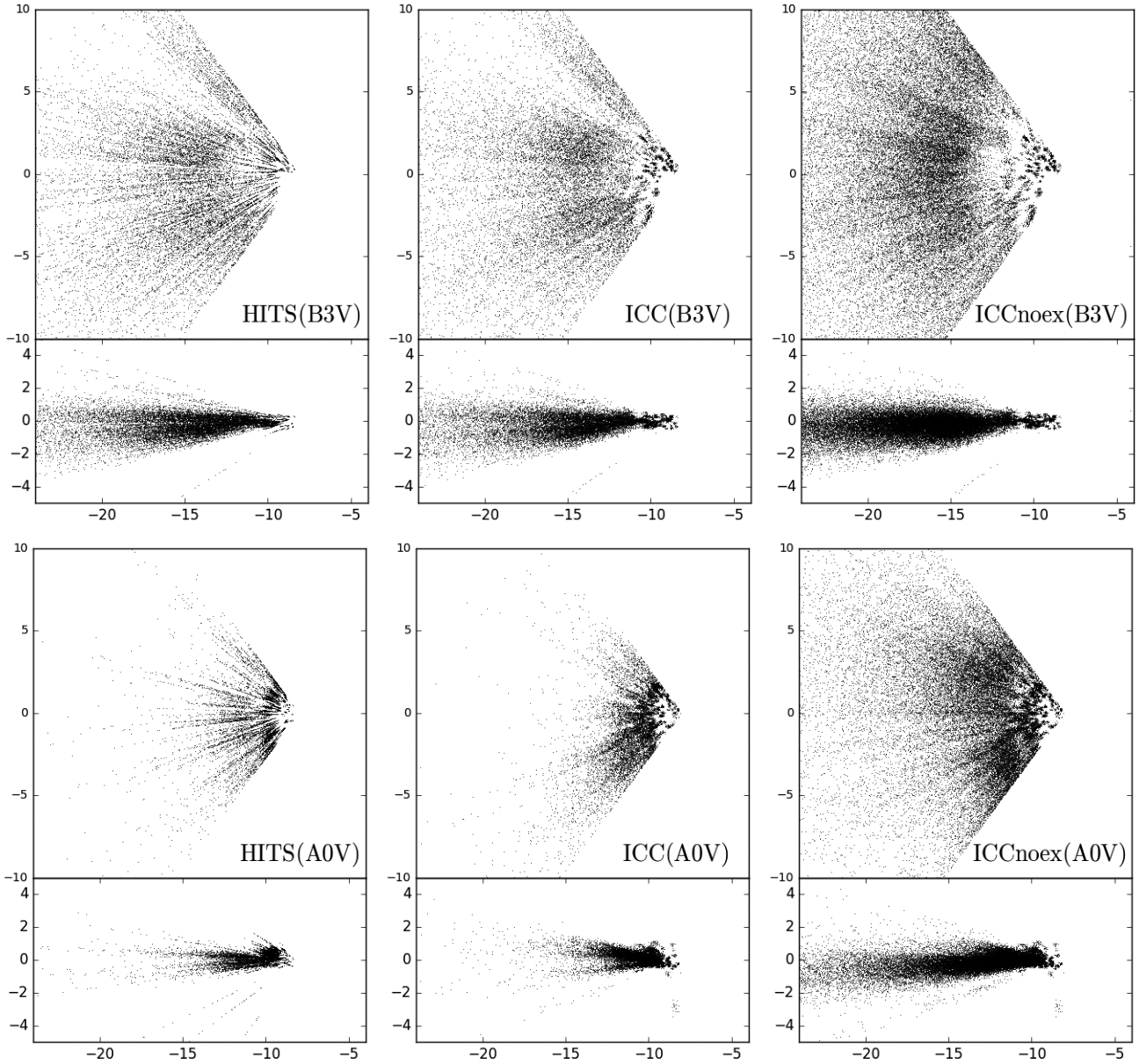

Figure 6. The face-on and edge-on distribution of B3V stars (top panels) and A0V stars (bottom panels) selected to be within a longitude of 126 deg $< l <$ 234 deg. This is shown for in the fiducial HITS-MOCK (left-hand panels), ICC-MOCK (middle panels), and ICC-MOCK-NOEX (right-hand panels) of Au 24. The Galactic Centre is located at $(X, Y, Z) = (-8, 0, 0.02)$ kpc. Note that the brighter B3V stars are spread over a larger portion of the disc than the A0V stars. The effects of dust extinction, particularly in the plane, are evident on comparison of the left-hand and middle panels with the right-hand panels and are more obvious for the A0V stars.

et al. (2018), who demonstrated that the vertical structure of polytropic, centrifugally supported gas discs with flat rotation curves embedded in CDM haloes naturally flare. Moreover, the recent controlled numerical study of Kawata et al. (2017) suggests that flaring star-forming regions are required in order to preserve a negative vertical metallicity gradient that would otherwise become positive owing to the outward radial migration of metal-rich stars. Flaring star-forming regions have therefore become a new and attractive way to help explain the flaring stellar disc.

A strong signature of an *in situ* flaring disc is a flaring distribution of very young stars ($\lesssim$ 300 Myr) because radial migration requires several dynamical times to become effective. We therefore select young A and B dwarf stars from the mock stellar catalogues according to the absolute V-band magnitude, $V - I_c$ colour, and tentative ages given by Pecaut & Mamajek (2013), that is: $(V, V - I_c) \sim (-1.1, -0.192)$ for B3V stars; and $(V, V - I_c) \sim (-1.11, 0.004)$ for A0V stars. These stars are typically $\sim$0.1 Gyr and $\sim$0.3 Gyr old, respectively. We select stars in the outer disc region (126 deg $< l <$ 234 deg) in order to minimize heavy mid-plane extinction. The distribution of stars is shown in Fig. 6 for each catalogue and demonstrates that these stars cover a significant portion of the outer disc, particularly in the absence of extinction. Comparison of the left-hand and middle panels with the right-hand panels of Fig. 6 highlights the drastically reduced number of stars near the disc mid-plane caused by dust extinction, particularly for A0V stars. The 'fingers of God' feature in the distributions shown in the HITS-MOCKS (left-hand panels of Fig. 6) is caused by fluctuations in dust attenuation along different lines of sight and by the displacement

of the true stellar positions along the line of sight due to parallax errors. These features are less evident in the ICC-MOCKS (middle panels of Fig. 6) because of the phase-space smoothing of the stars.

To make a simple estimate of the vertical thickness, we calculate the root mean square height (or scale height hereafter) as a function of observed Galactocentric radius for our samples of B3V and A0V stars, selected from mock catalogues generated for each simulation. The radial profiles of these scale heights are shown in Fig. 7 for the default solar position of 30 deg behind the major axis of the bar. In addition, we compare the scale height profiles of the B and A stars selected from each mock catalogue with those of raw simulation star particles of equivalent age. We show the profile given by the 'true' positions of the synthetic stars (before stars are displaced in phase space by errors), and the profile given by the 'observed' positions (after the stars have been displaced), for all mocks. Because both the true and observed positions in the ICC-MOCKS and HITS-MOCKS include extinction, the comparison of the true and observed profiles with the raw simulation data indicates the effects of the dust-corrected magnitude cut and errors separately in addition to their overall effect. However, the comparison of the ICC-MOCKS to the ICC-MOCKS-NOEX provides a direct indication of the effects of dust extinction. All mocks are affected by the magnitude cut.

The raw simulation data and the mock data exhibit flared vertical scale height profiles, and are, for the true mock data, in excellent agreement across the radial range 8–16 kpc for the B3V stars in all simulations. In most cases, the observed profiles are in good agreement with the raw simulation data, however, appreciable deviations begin to appear at heliocentric distances greater than ∼5 kpc for Au 16 and Au 23. This indicates that errors are more important than extinction for B-type dwarfs at these distances, which is confirmed by the distance error distributions shown in Fig. 8. The agreement is worse for the A0V stars compared to B3V stars at heliocentric distances larger than ∼4 kpc. Extinction (visible in the bottom-left and middle panels of Fig. 6) seems to be mainly responsible for the deviations away from the raw simulation data in these cases. This is reinforced by the ICC-MOCKS-NOEX profiles, which do not model extinction and generally reproduce well the raw simulation data even at galactocentric radii $\gtrsim$ 13 kpc for both types of stars. We note that the scale height profiles for the HITS-MOCKS and ICC-MOCKS are very similar for both stellar types.

In Fig. 9, we examine the radial profiles of the vertical velocity dispersion for the same stars as in Fig. 7. As expected from their flaring spatial distributions, the vertical velocity dispersion is nearly constant with radius in all cases, and is, in general, well reproduced by all mocks. Again, this is particularly true for B3V stars, which show minimal deviations, similar to those of their corresponding vertical scale height profiles. For A0V stars, the profiles are well reproduced up to heliocentric distances of ∼5 kpc, beyond which they begin to deviate noticeably in some cases. Apart from the increasing uncertainties in parallax and proper motion at these distances, an additional inaccuracy that contributes to the observed deviations is the lack of a radial velocity component in *Gaia* DR2 for these stars, although it is likely a minimal contribution for this application because radial velocities are almost perpendicular to the vertical velocity field at these low latitudes. The ICC-MOCKS-NOEX are able to reproduce the vertical velocity dispersion for both B3V and A0V stars very well and tend to bear out a more accurate representation of the dispersion at larger radii, where extinction begins to affect the HITS-MOCKS measurement of the A0V stars. Again, we note that the vertical velocity dispersion profiles for the HITS-MOCKS and ICC-MOCKS are very similar for both stellar types.

The results presented in Figs 7 and 9 demonstrate that, for *Gaia* DR2, BV and AV stars are reliable tracers for the very young stellar disc and, by extension, the distribution of star-forming regions; the intrinsic flaring of the star-forming gas disc is captured by these dwarf stars in both position and velocity space. It is worth to note that for subsequent data releases the reliability of these tracers will improve: The ability to trace the young disc will extend to the outer reaches of the disc and the warp beyond.

4.2 Stellar halo rotation

The spin of the Milky Way stellar halo is directly related to its merger history. To first order, the stellar halo rotation represents the net angular momentum of all of the Galaxy's past accretion events. Moreover, the presence of *in situ* halo stars, which are formed in the Galactic disc and later 'kicked out' into the halo due to merger events, can lead to disc-like kinematics in the stellar halo (i.e. net prograde rotation in the same sense as the disc, see e.g. McCarthy et al. 2012; Cooper et al. 2015; Pillepich, Madau & Mayer 2015). Thus, by measuring the net spin of the stellar halo we are probing the global accretion history of the Galaxy. In addition, we can gain further insight by measuring the halo rotation as a function of metallicity, Galactocentric radius, and position on the sky (see e.g. Carollo et al. 2007, 2010; Deason, Belokurov & Evans 2011; Hattori et al. 2013; Kafle et al. 2013).

Previous works attempting to measure the net spin of the halo have aimed to tease out the rotation signal using line-of-sight velocities from large spectroscopic samples of halo tracers (e.g. Sirko et al. 2004; Deason et al. 2011), this limitation to one velocity component is particularly troublesome for measuring rotation; at large distances the line-of-sight velocity is essentially the radial velocity component, and there is little, or no, constraint on the tangential velocity of halo stars. Prior to the *Gaia* era, reliable proper motion measures of distant halo stars were scarce, with ground-based samples subject to large-systematic uncertainties (e.g. Gould & Kollmeier 2004), and space-based samples limited to very small areas of the sky (Deason et al. 2013; Cunningham et al. 2016).

Now, in the era of *Gaia* DR2, we have access to all-sky proper motion measurements, with well-defined systematic and statistical error distributions. A prelude to the astrometric breakthrough from DR2 was presented in Deason et al. (2017), who used a proper motion catalogue constructed from SDSS images and *Gaia* DR1 to measure the net spin of the halo. The main drawback of the SDSS–*Gaia* proper motion catalogue is the constraint to the SDSS sky coverage, and the limited number of known halo tracers that could be used.

In this section, we use the mock catalogues to illustrate how *Gaia* DR2 astrometry can be used to measure the net spin of the stellar halo out to 100 kpc. The *Gaia* spacecraft is expected to observe $N \sim$ 70 000 Galactic halo RR Lyrae stars out to ∼100 kpc (Clementini et al. 2016). These old, metal-poor stars are approximate standard candles, and their distances can typically be measured with accuracies of less than 5 per cent (see e.g. Iorio et al. 2018). Here, we randomly sample $N \sim 70\,000$ 'old' (age > 9 Gyr) horizontal branch (HB) stars in the AURIGA haloes with $0 < B - V < 0.7$ and $0.2 < M_V < 1.2$. This selection was chosen to approximately mimic the all-sky RRL catalogues that will be released with *Gaia* DR2. To select halo stars, we include stars between 5 and 100 kpc from the Galactic Centre, and $|b| > 20$ deg above/below the disc plane, and height $|z| > 4$ kpc. We do not include distance uncertainties in the analysis (but note that including ∼5 per cent distance errors makes little difference to our results), and assume that while proper

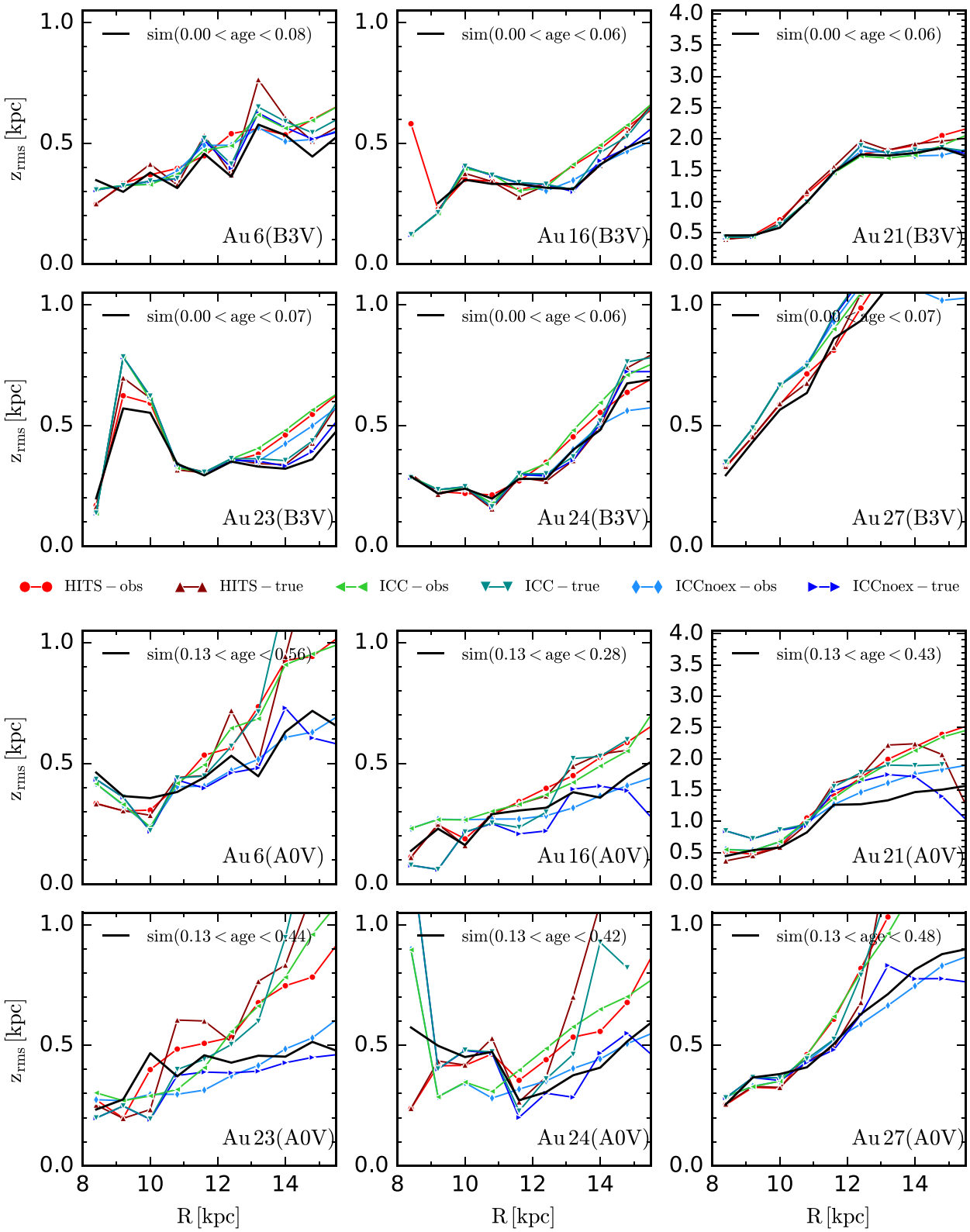

Figure 7. The root mean square vertical height as a function of radius for B3V dwarf stars (upper six panels) and A0V dwarf stars (lower six panels) from mock catalogues generated for each of the six simulations. The stars are selected in the outer disc (126 deg $< l <$ 234 deg) and around narrow M_V and $V - I_c$ ranges according to the values listed in Pecaut & Mamajek (2013). An additional cut on relative parallax error $0 < \sigma_\pi/\pi < 0.5$ is made. This typically results in several tens of thousands of stars that cover a large portion of the Galactic disc (see Fig. 6). In each case, we show the root mean square height of the raw simulation data for star particles of the corresponding age (black curves), the true positions of the HITS-MOCKS (red) and ICC-MOCKS with (green) and without (blue) extinction and the observed positions after error displacement (lighter colours) for each mock.

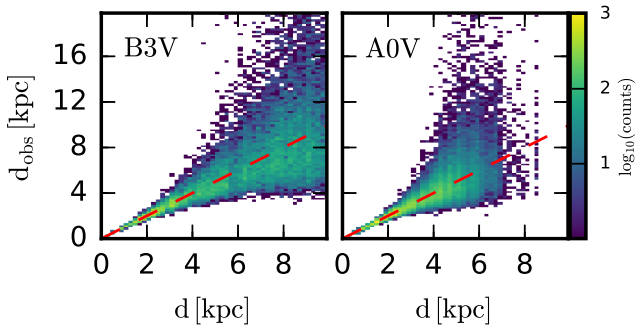

Figure 8. The observed heliocentric distance (after displacement from the parent star particle) as a function of real heliocentric distance (before displacement, i.e. the parent star particle distance) for B3V and A0V stars in the default HITS-MOCK of Au 24. The one-to-one relation is shown by the dashed red line.

motions measurements are available from *Gaia* DR2, there are no line-of-sight velocities.

In order to measure the halo rotation, we employ the same method introduced by Deason et al. (2017) to measure rotation with 5D data. In brief, we adopt a 3D velocity ellipsoid aligned in spherical coordinates, which assumes Gaussian velocity distributions and allows for net streaming in the v_ϕ component. A likelihood analysis is used to determine the best-fitting $\langle v_\phi \rangle$ value. For more details on this method, we refer the reader to Deason et al. (2017).

Fig. 10 shows the resulting mean rotation of stars in the radial range $r = 5{-}50$ kpc for six AURIGA haloes in HITS-MOCKS, ICC-MOCKS, and ICC-MOCKS-NOEX. The estimated $\langle v_\phi \rangle$ using the method of Deason et al. (2017), $v_{\phi,\rm est}$, is in very good agreement with the true value for the same samples of stars ($v_{\phi,\rm true}$). The errors on the mean values are smaller than the size of the symbols and therefore are omitted. The $v_{\phi,\rm true}$ values differ between the two mocks because different isochrones and IMFs are used, and thus our criteria for selecting old HB stars yield different subsets of stars. This point is important and illustrates that different subsets of old stars can have different rotation signals. We plan to investigate this further in a follow-up paper.

In Fig. 11, we show the estimated and true v_ϕ of our sample of old halo stars at different radii for all the mocks. The method of Deason et al. (2017) works very well at all radii to recover the actual spin of our samples of stars. It is remarkable that even at distances as large as 100 kpc, where *Gaia* proper motion errors are large and the number of stars is relatively small, one can recover the spin of the halo stars within $2-\sigma$. The spin profiles of raw star particles in the simulation are shown in this figure, as a reference, with a grey solid line. The particles are chosen to have the same spatial cut as the mock stars, but with age older than 10 Gyr; this is roughly equivalent to the colour–magnitude criteria we adopted to select HB stars. Slight differences between the profiles from mocks and simulations are expected as the sample of stars are different.

We note that Au 6 is the closest example to the MW according to halo spin, which was shown by Deason et al. (2017) to be in the range $\sim 0 - 20\,\mathrm{km\,s^{-1}}$ at galactocentric radii smaller than 50 kpc.

5 DISCUSSION AND CONCLUSIONS

We have presented several mock Milky Way stellar catalogues designed to match the selection criteria, volume, and observable properties (including uncertainties) of stars with $V < 16$ mag and $V < 20$ mag at $|b| > 20$ deg that will be provided by the *Gaia* data release 2. We employed two methods to calculate two sets of mock catalogues at four solar-like positions (equidistant in Galactic azimuth) from several high-resolution cosmological-zoom simulations: the HITS-MOCKS (generated with a parallelized version of SNAPDRAGONS, Hunt et al. 2015); and the ICC-MOCKS using the Lowing et al. (2015) method, which distributes stars in phase space by conserving the phase-space volume associated with each simulation stellar particle. Both sets of mocks take into account a simple dust extinction model; however, we produced also a full set of catalogues without extinction: ICC-MOCKS-NOEX. All mock catalogues provide *Gaia* DR2 data products: 6D phase-space information, magnitudes in the *Gaia* G-, $G_{\rm RP}$-, and $G_{\rm BP}$-photometric bands, effective temperature, and dust extinction values and include uncertainty estimates for the *Gaia* DR2 astrometric, photometric, and spectroscopic quantities. In addition, the catalogues provide the age, metallicity, mass, stellar surface gravity, gravitational potential, and photometry for non-*Gaia* bands for each of the generated stars. The catalogues are available online at both the AURIGA website and at the Durham database centre, the latter of which provides a query-based system to retrieve subsets of data. Gravitational potential grids and raw snapshot data for a subset of simulations are available for download at the AURIGA website.

5.1 Limitations

While the mock catalogues presented in this paper have great potential for helping to understand the formation of structure in our Milky Way in tandem with *Gaia* data, there are, of course, some limitations to each of the methods used to generate the catalogues.

Limitations of both methods: Neither method guarantees that the positions and velocities of mock stars are consistent with bound orbits in the simulation potential. Caution and careful sample selection based on filtering out stars with large errors should be followed for any of the applications that require precise correspondence between the motions of stars and their local gravitational potential, or that are sensitive to a small number of stars with very high velocities.

An important limitation worth bearing in mind is that the simulations have finite resolution. Even though the AURIGA project includes some of the highest resolution simulations of Milky Way analogues performed so far, a star particle represents a single stellar population of a few thousand solar masses. 'Exploding' these stellar particles into individual stars does not increase the resolution but allows a denser sampling of the phase space occupied by the original particles.

ICC-MOCKS limitations: Lowing et al. (2015) describe how the parameters entering the phase-space sampling step in the construction of the ICC-MOCKS were tuned to the values given in Section 3.3. This tuning sought to balance a sufficiently significant degree of expansion of stars away from their parent simulation particles against the preservation of coherent phase-space structures, such as tidal streams, and the suppression of bias in the bulk kinematics of the stellar halo. Lowing et al. (2015) studied collisionless N-body simulations, so the same approach and parameters are not guaranteed to be optimal for the massive, coherent baryonic discs in hydrodynamical simulations such as AURIGA. In particular, when we compute scale lengths for a star particle formed *in situ* in the main galaxy, we treat *all* the other *in situ* stars as its potential phase-space neighbours. This may be a substantial approximation because the set of all *in situ* particles comprises many different stellar populations that originate in different regions of phase space at different times. Treating all these as potential neighbours of one another can lead to 'cross-talk' between distinct dynamical structures, a form of over-

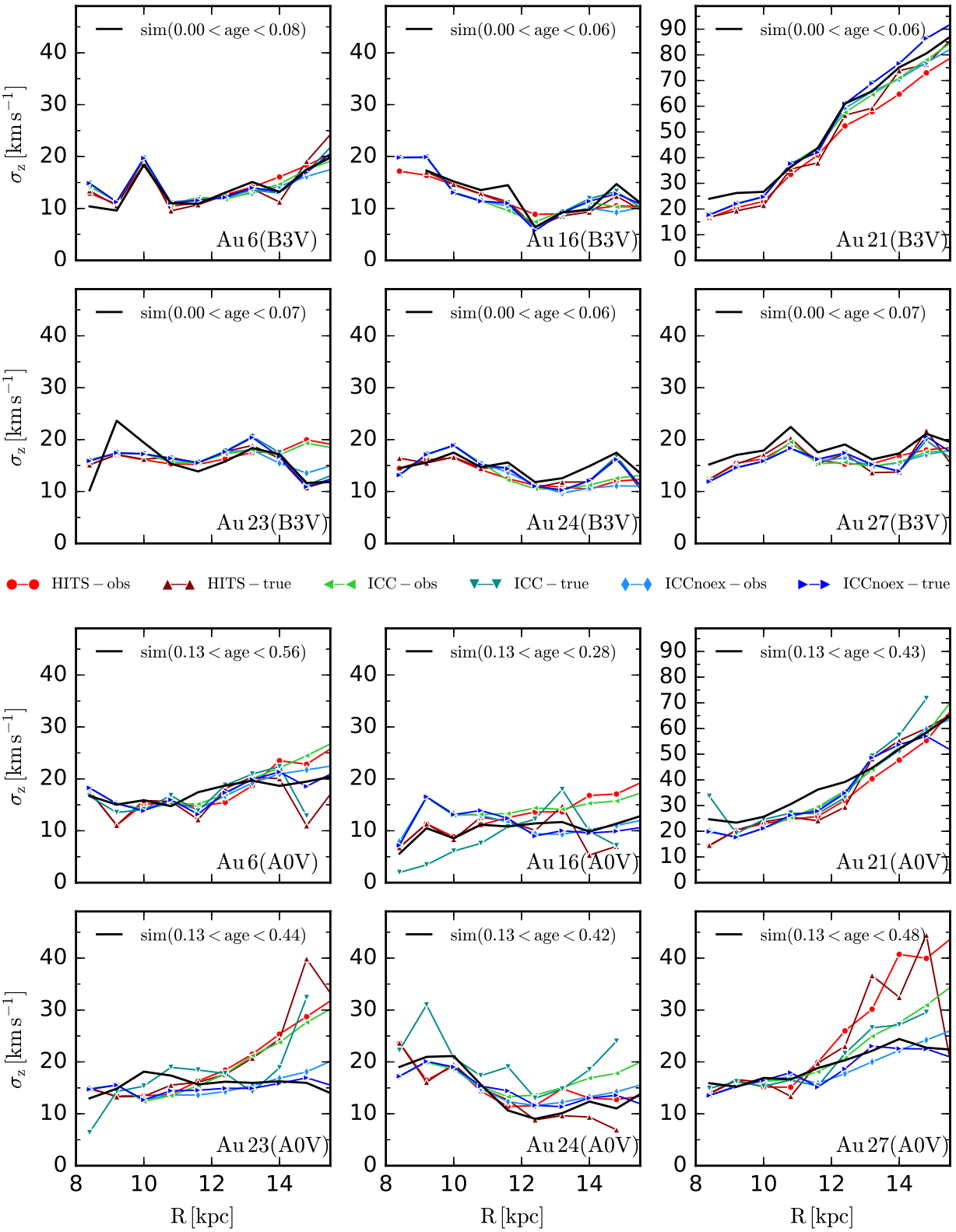

Figure 9. As Fig. 7 but for the vertical velocity dispersion.

smoothing (which is mitigated in the case of accreted halo stars by only considering particles from the same progenitor satellite as potential neighbours). For example, the scale height and vertical velocity dispersion of young, kinematically cold stars in the disc may (in principle) be inflated if neighbours from a kinemtically hotter bulk population dominate the kernels associated with their parent particles. However, in practice, we see no evidence of any significant bias in the analyses of young disc stars we present here.

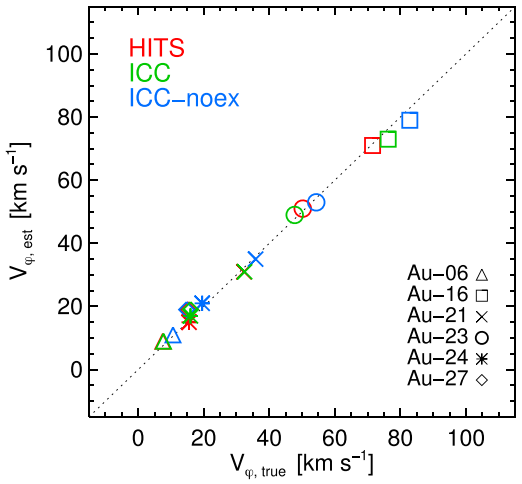

Figure 10. Estimated mean V_ϕ, based on the method of Deason et al. (2017) from 5D data of a random sample of 70 000 HB halo stars in HITS-MOCKS (red), ICC-MOCKS (blue), and ICC-MOCKS-NOEX (green), versus the true mean V_ϕ calculated from the 6D phase-space information of the same samples. The different symbol types represent the six AURIGA simulations for which the mock catalogues are created as indicated in the legend.

The possibility of artefacts arising from the phase-space sampling procedure should be kept in mind nevertheless, especially in applications that probe phase-space structure on very small scales.

HITS-MOCKS limitations: The HITS-MOCKS do not include a phase-space sampling step, i.e. the generated stars are not interpolated in phase space, before adding *Gaia* DR2 errors to the particle phase-space coordinates. This may create artefacts for structures that are 'long' and 'thin', such as the great circle stream, that arise from the displacement of stars along the line of sight with very similar celestial coordinates. Furthermore, the observed positions generated by displacing the coordinates of the parent star particle can be spread over large ranges for particles beyond ∼10 kpc heliocentric distances, where the errors become large. This means that using parallax distances for some halo stars directly can become unreliable, and more sophisticated approaches, such as the one used in this paper, are required.

We conclude that the ICC-MOCKS are perhaps better suited than the HITS-MOCKS for studying streams, other inhomogeneities and debris in the stellar halo, owing to the refined phase-space sampling. Both sets of mocks include a model for dust extinction that allows the user to make quick assessments of how dust affects *Gaia* observables, which is particularly important for the stellar disc. Conversely, the ICC-MOCKS-NOEX provide the user freedom to add any dust model to the data. The mock catalogues presented in this paper are therefore

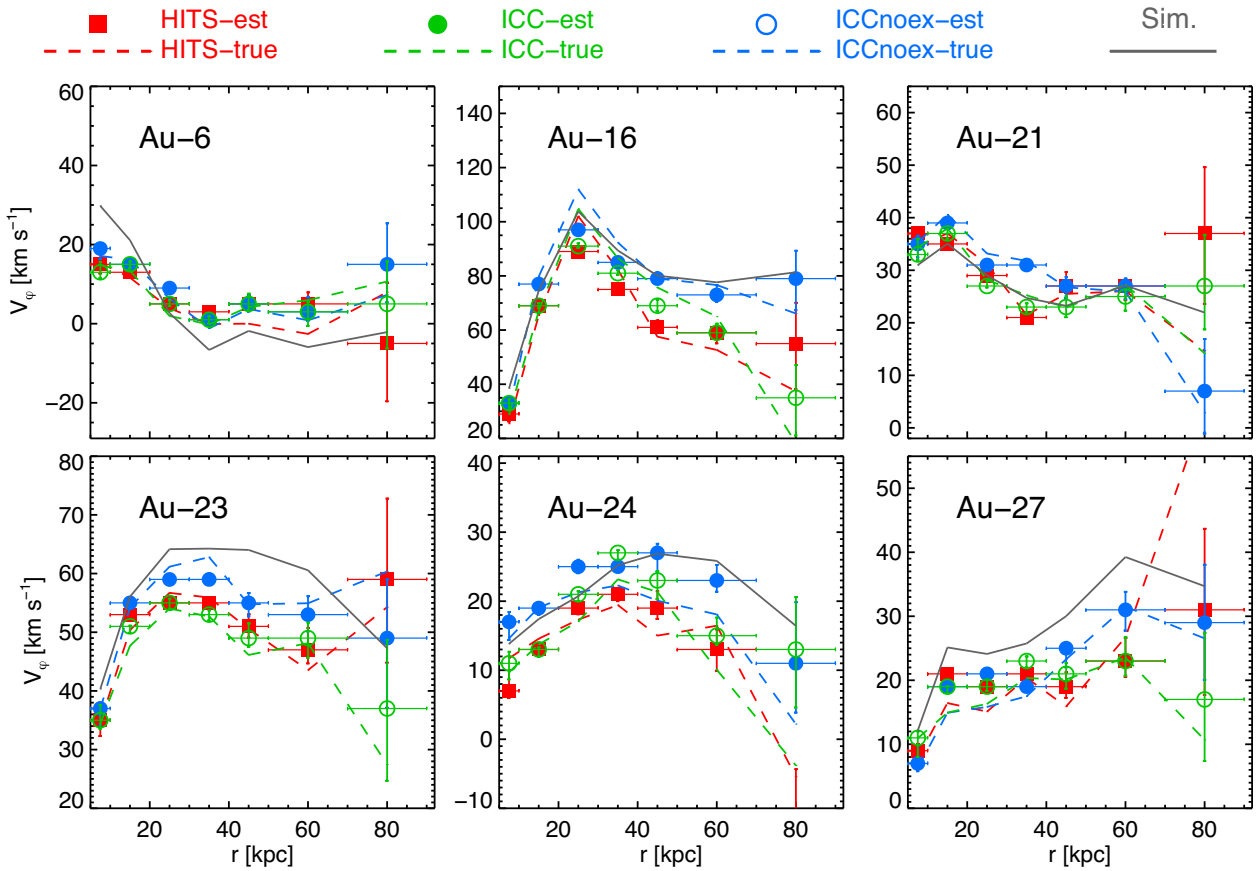

Figure 11. Estimated V_ϕ from 5D data of HB halo stars at different galactocentric radial bins for AURIGA galaxies compared to the true V_ϕ of the same samples. The red, green, and blue colours correspond to HITS-MOCKS, ICC-MOCKS, and ICC-MOCKS-NOEX, respectively. Different symbol types represent estimated values, while the true values are shown with dashed lines. The horizontal error bars illustrate the size of the radial bins, while the vertical error bars show the error in the mean values. The profile of raw simulated star particles, with a spatial cut similar to that in the mock catalogues and age >10 Gyr, is shown with a solid grey line, for reference.

complementary and provide a wide scope for assessing the biases and capabilities of the *Gaia* DR2.

We note that the codes used to generate these mock catalogues may be improved in the future, in which case the mock catalogues on our public data base will be updated accordingly. We urge users to refer back to the data base whenever a new application is considered.

5.2 Applications

As a first science application of the mocks, we analysed the vertical structure of the young stellar disc and found that all simulations showed a flaring vertical scale height profile with a consistently flat vertical velocity dispersion profile. We verified that B3V and A0V stars in the outer disc selected from the mock catalogues reproduce these trends; young B and A dwarf star data in DR2 should be reliable tracers of the young stellar disc. If in the *Gaia* DR2 data these tracers exhibit flaring profiles, this will constitute evidence for flaring star-forming regions and perhaps indicate that radial migration and dynamical heating from satellite perturbations are not the principal drivers of the flaring mono-abundance populations found in other Galactic surveys (Bovy et al. 2016; Mackereth et al. 2017).

We also applied the method of Deason et al. (2017) to samples of old HB halo stars in the mock catalogues to estimate the mean rotation of AURIGA stellar haloes based on 5D phase-space information. We find excellent agreement between the estimated mean rotation velocity and the true values, even at galactocentric distances as large as 100 kpc. The results show that accurate distance measurements combined with proper motions from *Gaia*, can reliably predict the mean rotation of halo stars. Obtaining an accurate estimate of the spin of the distant MW stellar halo is therefore extremely promising using the tens of thousands of RR Lyrae stars that *Gaia* will provide.

The mock catalogues presented in this paper are the first such catalogues generated from *ab initio* high-resolution ΛCDM galaxy formation simulations; they offer a novel perspective of the Milky Way and may be used for a variety of applications. In particular, they provide a testbed for the design and evaluation of Galaxy modelling methods in a realistic cosmological setting, a means to gauge the limitations and biases of *Gaia* DR2 and to link observations to theoretical predictions, encapsulated in the simulations, enabling robust inferences to be made about the multitude of galaxy formation processes that shaped the Milky Way.

ACKNOWLEDGEMENTS

The authors thank the referee for a constructive and helpful report that led to the improvement of the manuscript. RG would like to thank Daisuke Kawata for many useful discussions. RG and VS acknowledge support by the Deutsche Forschungsgemeinschaft (DFG) Research Centre SFB-881 'The Milky Way System' through project A1. JASH is supported by a Dunlap Fellowship at the Dunlap Institute for Astronomy & Astrophysics, funded through an endowment established by the Dunlap family and the University of Toronto. AD is supported by a Royal Society University Research Fellowship. AF is supported by a European Union COFUND/Durham Junior Research Fellowship (under EU grant agreement no. 609412). MC was supported by Science and Technology Facilities Council (STFC) [ST/P000541/1]. FAG acknowledges support from Fondecyt Regular 1181264. This work has also been supported by the European Research Council under ERC-StG grant EXAGAL- 308037 and the Klaus Tschira Foundation. Part of the simulations of this paper used the SuperMUC system at the Leibniz Computing Centre, Garching, under the project PR85JE of the Gauss Centre for Supercomputing. This work used the DiRAC Data Centric system at Durham University, operated by the Institute for Computational Cosmology on behalf of the STFC DiRAC High Performance Computing Facility www.dirac.ac.uk. This equipment was funded by BIS National E-infrastructure capital grant ST/K00042X/1, STFC capital grant ST/H008519/1, and STFC DiRAC Operations grant ST/K003267/1 and Durham University. DiRAC is part of the National E-Infrastructure.

REFERENCES

Bahcall J. N., Soneira R. M., 1980, ApJS, 44, 73
Bailer-Jones C. A. L., 2011, MNRAS, 411, 435
Bell E. F., Monachesi A., Harmsen B., de Jong R. S., Bailin J., Radburn-Smith D. J., D'Souza R., Holwerda B. W., 2017, ApJ, 837, L8
Benítez-Llambay A., Navarro J. F., Frenk C. S., Ludlow A. D., 2018, MNRAS, 473, 1019
Bienayme O., Robin A. C., Creze M., 1987, A&A, 180, 94
Binney J., 2010, MNRAS, 401, 2318
Binney J., McMillan P. J., 2016, MNRAS, 456, 1982
Bland-Hawthorn J., Gerhard O., 2016, ARA&A, 54, 529
Bland-Hawthorn J., Krumholz M. R., Freeman K., 2010, ApJ, 713, 166
Bondi H., 1952, MNRAS, 112, 195
Bondi H., Hoyle F., 1944, MNRAS, 104, 273
Bovy J., Rix H.-W., 2013, ApJ, 779, 115
Bovy J., Rix H.-W., Hogg D. W., 2012, ApJ, 751, 131
Bovy J., Rix H.-W., Schlafly E. F., Nidever D. L., Holtzman J. A., Shetrone M., Beers T. C., 2016, ApJ, 823, 30
Bressan A., Marigo P., Girardi L., Salasnich B., Dal Cero C., Rubele S., Nanni A., 2012, MNRAS, 427, 127
Bruzual G., Charlot S., 2003, MNRAS, 344, 1000
Bullock J. S., Johnston K. V., 2005, ApJ, 635, 931
Campante T. L. et al., 2016, ApJ, 830, 138
Carollo D. et al., 2007, Nature, 450, 1020
Carollo D. et al., 2010, ApJ, 712, 692
Chabrier G., 2003, PASP, 115, 763
Chen L. et al., 2012, Res. Astron. Astrophys., 12, 805
Chen Y., Girardi L., Bressan A., Marigo P., Barbieri M., Kong X., 2014, MNRAS, 444, 2525
Chen Y., Bressan A., Girardi L., Marigo P., Kong X., Lanza A., 2015, MNRAS, 452, 1068
Clementini G. et al., 2016, A&A, 595, A133
Cole S. et al., 2005, MNRAS, 362, 505
Cooper A. P. et al., 2010, MNRAS, 406, 744
Cooper A. P., Parry O. H., Lowing B., Cole S., Frenk C., 2015, MNRAS, 454, 3185
Cunningham E. C. et al., 2016, ApJ, 820, 18
Deason A. J., Belokurov V., Evans N. W., 2011, MNRAS, 411, 1480
Deason A. J., Van der Marel R. P., Guhathakurta P., Sohn S. T., Brown T. M., 2013, ApJ, 766, 24
Deason A. J., Belokurov V., Koposov S. E., Gómez F. A., Grand R. J., Marinacci F., Pakmor R., 2017, MNRAS, 470, 1259
DESI Collaboration, 2016, preprint (arXiv:1611.00036)
Fattahi A. et al., 2016, MNRAS, 457, 844
Faucher-Giguère C.-A., Lidz A., Zaldarriaga M., Hernquist L., 2009, ApJ, 703, 1416
Fragkoudi F., Di Matteo P., Haywood M., Gómez A., Combes F., Katz D., Semelin B., 2017, A&A, 606, A47
Gaia Collaboration, 2016, A&A, 595, A1
Gaia Collaboration, 2018a, A&A, 616, A12
Gaia Collaboration, 2018b, A&A, 616, A11
Gaia Collaboration, 2018c, A&A, 616, A10
Gaia Collaboration, 2018d, A&A, 616, A1
Garrison-Kimmel S. et al., 2017, preprint (arXiv:1712:03966)

Gilmore G. et al., 2012, The Messenger, 147, 25
Gómez F. A., White S. D. M., Grand R. J. J., Marinacci F., Springel V., Pakmor R., 2017, MNRAS, 465, 3446
Gould A., Kollmeier J. A., 2004, ApJS, 152, 103
Grand R. J. J., Kawata D., Cropper M., 2012, MNRAS, 426, 167
Grand R. J. J., Kawata D., Cropper M., 2013, A&A, 553, A77
Grand R. J. J., Springel V., Gómez F. A., Marinacci F., Pakmor R., Campbell D. J. R., Jenkins A., 2016, MNRAS, 459, 199
Grand R. J. J. et al., 2017, MNRAS, 467, 179
Grand R. J. J. et al., 2018, MNRAS, 474, 3629
Guo Q., White S., Li C., Boylan-Kolchin M., 2010, MNRAS, 404, 1111
Hattori K., Yoshii Y., Beers T. C., Carollo D., Lee Y. S., 2013, ApJ, 763, L17
Hayden M. R. et al., 2015, ApJ, 808, 132
Hunt J. A. S., Kawata D., 2013, MNRAS, 430, 1928
Hunt J. A. S., Kawata D., 2014, MNRAS, 443, 2112
Hunt J. A. S., Kawata D., Grand R. J. J., Minchev I., Pasetto S., Cropper M., 2015, MNRAS, 450, 2132
Iorio G., Belokurov V., Erkal D., Koposov S. E., Nipoti C., Fraternali F., 2018, MNRAS, 474, 2142
Jenkins A., 2010, MNRAS, 403, 1859
Jordi C. et al., 2010, A&A, 523, A48
Kafle P. R., Sharma S., Lewis G. F., Bland-Hawthorn J., 2013, MNRAS, 430, 2973
Katz N., Gunn J. E., 1991, ApJ, 377, 365
Kawata D., Grand R. J. J., Gibson B. K., Casagrande L., Hunt J. A. S., Brook C. B., 2017, MNRAS, 464, 702
Kroupa P., 2001, MNRAS, 322, 231
Kulsrud R. M., Zweibel E. G., 2008, Rep. Prog. Phys., 71, 046901
Liu C., Bailer-Jones C. A. L., Sordo R., Vallenari A., Borrachero R., Luri X., Sartoretti P., 2012, MNRAS, 426, 2463
Lowing B., Wang W., Cooper A., Kennedy R., Helly J., Cole S., Frenk C., 2015, MNRAS, 446, 2274
Mackereth J. T. et al., 2017, MNRAS, 471, 3057
Majewski S. R. et al., 2017, AJ, 154, 94
Marigo P., Girardi L., Bressan A., Groenewegen M. A. T., Silva L., Granato G. L., 2008, A&A, 482, 883
Marinacci F., Vogelsberger M., 2016, MNRAS, 456, L69
Marinacci F., Pakmor R., Springel V., 2014, MNRAS, 437, 1750
Marinacci F., Vogelsberger M., Mocz P., Pakmor R., 2015, MNRAS, 453, 3999
Martell S. L. et al., 2017, MNRAS, 465, 3203
Martig M., Minchev I., Flynn C., 2014, MNRAS, 443, 2452
Mateu C., Cooper A. P., Font A. S., Aguilar L., Frenk C., Cole S., Wang W., McCarthy I. G., 2017, MNRAS, 469, 721
McCarthy I. G., Font A. S., Crain R. A., Deason A. J., Schaye J., Theuns T., 2012, MNRAS, 420, 2245
McMillan P. J., 2011, MNRAS, 414, 2446
Minchev I., Famaey B., Quillen A. C., Dehnen W., Martig M., Siebert A., 2012, A&A, 548, A127
Minchev I., Chiappini C., Martig M., 2014a, A&A, 572, A92
Minchev I. et al., 2014b, ApJ, 781, L20
Monachesi A., Gómez F. A., Grand R. J. J., Kauffmann G., Marinacci F., Pakmor R., Springel V., Frenk C. S., 2016, MNRAS, 459, L46
Monachesi A. et al., 2018, MNRAS, preprint (arXiv:1804.07798)
Navarro J. F., Steinmetz M., 2000, ApJ, 538, 477
Navarro J. F. et al., 2018, MNRAS, 476, 3648
Nulsen P. E. J., Fabian A. C., 2000, MNRAS, 311, 346
Okamoto T., Frenk C. S., Jenkins A., Theuns T., 2010, MNRAS, 406, 208
Pakmor R., Springel V., 2013, MNRAS, 432, 176
Pakmor R., Marinacci F., Springel V., 2014, ApJ, 783, L20
Pakmor R. et al., 2017, MNRAS, 469, 3185
Pecaut M. J., Mamajek E. E., 2013, ApJS, 208, 9
Pillepich A., Madau P., Mayer L., 2015, ApJ, 799, 184
Planck Collaboration XVI, 2014, A&A, 571, A16
Quinn P. J., Hernquist L., Fullagar D. P., 1993, ApJ, 403, 74
Rahimi A., Carrell K., Kawata D., 2014, Res. Astron. Astrophys., 14, 1406
Rauer H. et al., 2014, Exp. Astron., 38, 249
Rix H.-W., Bovy J., 2013, A&AR, 21, 61
Robin A., Creze M., 1986, A&A, 157, 71
Robin A. C., Reylé C., Derrière S., Picaud S., 2003, A&A, 409, 523
Robin A. C. et al., 2012, A&A, 543, A100
Romero-Gómez M., Figueras F., Antoja T., Abedi H., Aguilar L., 2015, MNRAS, 447, 218
Roškar R., Debattista V. P., Loebman S. R., 2013, MNRAS, 433, 976
Rybizki J., Demleitner M., Fouesneau M., Bailer-Jones C., Rix H.-W., Andrae R., 2018, PASP, 130, 074101
Salpeter E. E., 1955, ApJ, 121, 161
Sawala T. et al., 2015, MNRAS, 448, 2941
Scannapieco C., White S. D. M., Springel V., Tissera P. B., 2011, MNRAS, 417, 154
Schaye J. et al., 2015, MNRAS, 446, 521
Schlegel D. J., Finkbeiner D. P., Davis M., 1998, ApJ, 500, 525
Schönrich R., Binney J., 2009, MNRAS, 396, 203
Schönrich R., McMillan P. J., 2017, MNRAS, 467, 1154
Schönrich R., Binney J., Dehnen W., 2010, MNRAS, 403, 1829
Sharma S., Steinmetz M., 2006, MNRAS, 373, 1293
Sharma S., Bland-Hawthorn J., Johnston K. V., Binney J., 2011, ApJ, 730, 3
Simpson C. M., Grand R. J. J., Gómez F. A., Marinacci F., Pakmor R., Springel V., Campbell D. J. R., Frenk C. S., 2018, MNRAS, 478, 548
Sirko E. et al., 2004, AJ, 127, 899
Solway M., Sellwood J. A., Schönrich R., 2012, MNRAS, 422, 1363
Springel V., 2010, MNRAS, 401, 791
Springel V., Hernquist L., 2003, MNRAS, 339, 289
Springel V., Di Matteo T., Hernquist L., 2005, MNRAS, 361, 776
Springel V. et al., 2008, MNRAS, 391, 1685
Stello D. et al., 2017, ApJ, 835, 83
Syer D., Tremaine S., 1996, MNRAS, 282, 223
Tang J., Bressan A., Rosenfield P., Slemer A., Marigo P., Girardi L., Bianchi L., 2014, MNRAS, 445, 4287
Trayford J. W. et al., 2017, MNRAS, 470, 771
Trick W. H., Bovy J., Rix H.-W., 2016, ApJ, 830, 97
Vogelsberger M., Genel S., Sijacki D., Torrey P., Springel V., Hernquist L., 2013, MNRAS, 436, 3031
Wang L., Dutton A. A., Stinson G. S., Macciò A. V., Penzo C., Kang X., Keller B. W., Wadsley J., 2015, MNRAS, 454, 83
de Jong R. S. et al., 2014, in Ramsay S. K. , McLean I. S., Takami H., eds, Proc. SPIE Conf. Ser. Vol. 9147, Ground-based and Airborne Instrumentation for Astronomy V. SPIE, Bellingham, p. 91470M
van Leeuwen F., Feast M. W., Whitelock P. A., Laney C. D., 2007, MNRAS, 379, 723

APPENDIX A: FIELDS AND UNITS OF THE MOCK CATALOGUES

The mock catalogues are in hdf5 file format and can be downloaded in their entirety or queried through an SQL database system at http://data.cosma.dur.ac.uk:8080/gaia-mocks/. The data products and units are listed in each catalogue file and are listed in Table A1. A basic PYTHON script to read the mock data and perform coordinate transformations and example SQL queries are provided on the AURIGA website http://auriga.h-its.org.

Table A1. Description of the data products and their units of the mock catalogues. Quantities denoted [a] and [b] are present in the HITS-MOCKS and ICC-MOCKS only, respectively. For clarity, α, δ, and π are the right ascension, declination, and parallax, respectively, and μ^*_α, μ_δ, and v_r are the proper motion right ascension in true arc ($\mu^*_\alpha = \mu_\alpha \cos(\delta)$), the proper motion declination and heliocentric radial velocities, respectively.

Catalogue field name	Units	Description
AccretedFlag	–	equal to either (-1, 0, 1) for (*in situ*, accreted, in existing subhalo)
Age	gigayears	the look back time at which the parent star particle is born
EffectiveTemperature	Kelvin	the true effective temperature of the synthetic star
EffectiveTemperatureError	Kelvin	the error in effective temperature of the synthetic star
EffectiveTemperatureObs	Kelvin	the observed effective temperature of the synthetic star
[a]Extinction31	magnitudes	*V*-band extinction value
GBmagnitude	magnitudes	true *Gaia* blue G_B-band luminosity
GBmagnitudeError	magnitudes	error in *Gaia* blue G_B-band luminosity
GBmagnitudeObs	magnitudes	observed *Gaia* blue G_B-band luminosity
GRmagnitude	magnitudes	true *Gaia* red G_R-band luminosity
GRmagnitudeError	magnitudes	error in *Gaia* red G_R-band luminosity
GRmagnitudeObs	magnitudes	observed *Gaia* red G_R-band luminosity
Gmagnitude	magnitudes	true *Gaia* white light *G*-band luminosity
GmagnitudeError	magnitudes	error in *Gaia* white light *G*-band luminosity
GmagnitudeObs	magnitudes	observed *Gaia* white light *G*-band luminosity
GravPotential	$\mathrm{km^2\,s^{-2}}$	gravitational potential of the parent star particle
HCoordinateErrors	(radians, radians, arcsec)	2D array of errors in (α, δ, π)
HCoordinates	(radians, radians, arcsec)	2D array of true (α, δ, π)
HCoordinatesObs	(radians, radians, arcsec)	2D array of observed (α, δ, π)
HVelocities	($\mathrm{arcsec\,yr^{-1}}$, $\mathrm{arcsec\,yr^{-1}}$, $\mathrm{km\,s^{-1}}$)	2D array of true (μ^*_α, μ_δ, v_r)
HVelocitiesObs	($\mathrm{arcsec\,yr^{-1}}$, $\mathrm{arcsec\,yr^{-1}}$, $\mathrm{km\,s^{-1}}$)	2D array of observed (μ^*_α, μ_δ, v_r)
HVelocityErrors	($\mathrm{arcsec\,yr^{-1}}$, $\mathrm{arcsec\,yr^{-1}}$, $\mathrm{km\,s^{-1}}$)	2D array of errors in (μ^*_α, μ_δ, v_r)
IabsMagnitude	magnitudes	*I*-band absolute magnitude
Magnitudes	(magnitudes)$\times$ 8	2D array of apparent magnitudes in the (U, B, R, J, H, K, V, I) bands
[b]InitialMass	solar masses	mass of the star when it was born (before mass-loss occurs)
Mass	solar masses	mass of the star
Metallicity	–	metallicity of the star
ParticleID	–	unique ID of the parent particle
SurfaceGravity	log	logarithm of the true surface gravity of the star
SurfaceGravityError	log	logarithm of the error in surface gravity of the star
SurfaceGravityObs	log	logarithm of the observed surface gravity of the star
VabsMagnitude	magnitudes	*V*-band absolute magnitude

This paper has been typeset from a TEX/LATEX file prepared by the author.